Silicon Oxynitride Coatings Are Very Promising for Inert and Durable Pharmaceutical Glass Vials

Konstantina Christina Topka, Babacar Diallo, Maxime Puyo, Erwan Chesneau, Farah Inoubli, Simon Ponton, Cecile Genevois, Diane Samelor, Raphaël Laloo, Daniel Sadowski, et al.

▶ To cite this version:

Konstantina Christina Topka, Babacar Diallo, Maxime Puyo, Erwan Chesneau, Farah Inoubli, et al.. Silicon Oxynitride Coatings Are Very Promising for Inert and Durable Pharmaceutical Glass Vials. ACS Applied Engineering Materials, In press, 1 (10), pp.2707-2722. ⟨10.1021/acsaenm.3c00584⟩. ⟨hal-04336271⟩

HAL Id: hal-04336271
https://hal.science/hal-04336271v1

Submitted on 11 Dec 2023

ACS APPLIED ENGINEERING MATERIALS

Silicon Oxynitride Coatings Are Very Promising for Inert and Durable Pharmaceutical Glass Vials

Konstantina Christina Topka, Babacar Diallo, Maxime Puyo, Erwan Chesneau, Farah Inoubli, Simon Ponton, Cecile Genevois, Diane Samelor, Raphael Laloo, Daniel Sadowski, Cédric Charvillat, Takashi Teramoto, François Senocq, Thierry Sauvage, Hugues Vergnes, Marie-Joelle Menu, Christian Dussarrat, Brigitte Caussat, Viviane Turq, Constantin Vahlas, and Nadia Pellerin*

Cite This: https://doi.org/10.1021/acsaenm.3c00584 Read Online

ACCESS | Metrics & More | Article Recommendations | Supporting Information

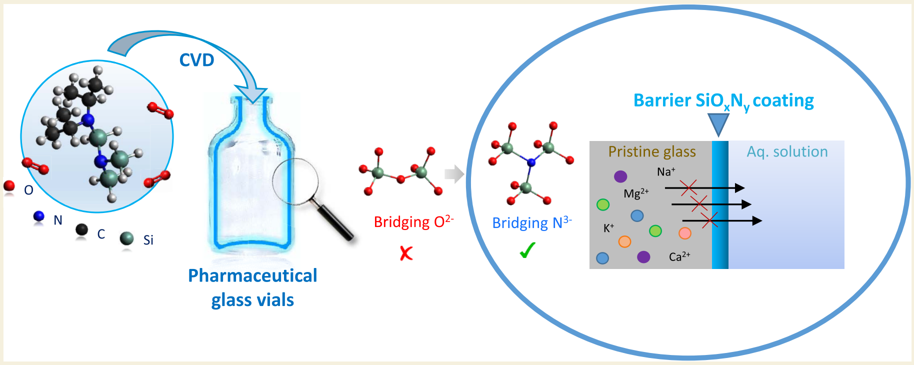

ABSTRACT: Glass packaging of novel medicinal molecules is challenged by hydrolysis of the glass network from an interaction with the stored drug, likely to result in leaching of constituent elements of the glass into the solution. We have succeeded in applying chemical-vapor-deposited silicon oxynitride coatings from a highly reactive trisilylamine derivative molecule as a precursor, at a temperature below 580 °C, opening up the possibility utilizing such coatings on glass surfaces. We demonstrate that such silicon oxynitride coatings applied on the internal surface of pharmaceutical vials prevent degradation, providing chemical inertness and withstanding severe screening conditions of the United States Pharmacopeia USP <1660> chapter. Fine structural determination and atomistic modeling of the Si−O−N network of the films confirm the nitrogen substitution of oxygen and densification of the silicate network through the addition of the former. The achieved barrier properties and excellent performance of these coatings pave the way toward sustainable packaging with improved product shelf life, transferable to multiple applications of surface coatings.

KEYWORDS: *silicon oxynitride coatings, corrosion barrier, pharmaceutical vials, USP <1660>, chemical vapor deposition*

INTRODUCTION

Recent developments in the pharmaceutical industry highlighted challenges regarding sustainable packaging of drugs derived from new molecular entities and delicate active pharmaceutical ingredients.[1,2] A commentary published during the first few months of the COVID-19 pandemic underscored the enormous need for billions of vials to contain coronavirus vaccine doses and praised the appropriateness of glass, the primary packaging of choice, particularly due to its superior long-term storage and low gas permeability.[3] Nonetheless, silicate glass is chemically reactive vis à vis aqueous phases despite its apparent chemical inertness.[4,5] This extremely slow but inexorable glass surface dissolution can adopt different mechanisms of ion exchange and surface hydration, which leads from alkali-depleted layers, up to hydrolysis of the silicon−oxygen bonds, subsequently inducing thickness loss by network dissolution, especially in basic media.[6−8] These mechanisms depend not only on the glass composition and network structure but also on the solution in contact with the glass surface. Reactive excipient solutions in which molecular entities are conditioned can still interact aggressively with the glass container,[9] altering the glass surface, and ultimately producing a silica-rich gel layer likely to detach from the surface, or precipitate particles from the ions in solution and constituents of the drug product, pitting, or glass flakes (lamellae) through delamination, as exemplified by the

Received: September 25, 2023
Revised: October 24, 2023
Accepted: October 25, 2023

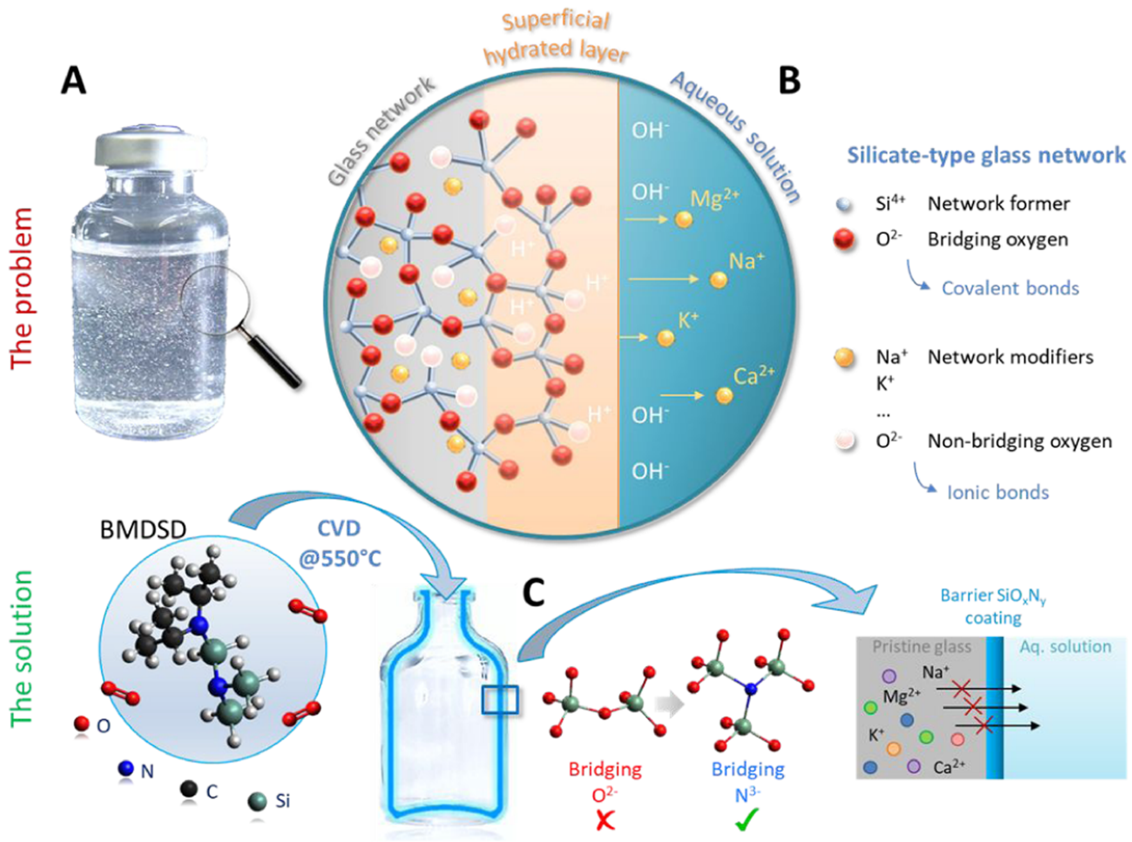

Figure 1. Hydrolysis phenomenon of the internal glass surface and the proposed remediation approach. (A) Photograph of a vial showing the release of delaminated glass fragments in a stored liquid medium. Photo courtesy of SCHOTT pharma services. (B) Schematic of the silicate-type glass network and its superficial alteration upon contact with aqueous solutions. The alteration is initiated by the formation of a hydrated layer followed by the release of alkali cations in the solution with a subsequent increase in pH. (C) Thermal CVD process involving the *N*,*N*-bis(1-methylethyl)-*N*′,*N*′-disilyl-silanediamine (BMDSD) precursor (lower left), yielding highly resistant SiO_xN_y coatings on the internal surface of glass vials.

photograph of Figure 1A. As a result, the integrity of the vial surface is reduced, leading to contamination of the drug product.[10,11] The borosilicate glass delamination is particularly sensitive to the glass vial manufacturing process and is assumed to occur mostly in areas where extensive heat treatment was applied during the vial-forming process such as the bottom and shoulder.[2,12] This heat treatment, applied in particular during the tubular converting process, results in the evaporation of alkali and borates and then their deposition, which induces a boron- and sodium-enriched region with a lower chemical durability.[10] But other parameters can also influence this delamination complex phenomenon such as sterilization, washing and depyrogenation steps, surface/volume ratio, solution pH, buffer components such as phosphate, citrate, tartrate, and alkaline, or temperature of storage.[2] Moreover, delamination takes a long time to appear, on the order of months or years of drug storage. However, extreme stress conditions applied to glass containers can accelerate the glass delamination and assess the potential for delamination for a given chemical medium.[12] The informal monograph in the United States Pharmacopoeia USP <1660> provides guidance to the pharmaceutical industry for evaluating glass delamination and more globally, glass hydrolytic resistance, through severe chemical tests in basic media. These tests simulate an accelerated aging compared to room-temperature storage. However, withstanding severe USP <1660> tests does not guarantee the absence of delamination for a given drug product, just as failure to pass these tests does not mean that the glass surface in contact with the drug will develop delamination.

Resistance to alteration in aqueous media of both borosilicate (Type I) and soda-lime (Type III) glasses is being pushed to its limits considering the ability of the Si−O covalent bonds to resist hydrolysis, given by the activation energy for hydrolysis.[13−15] This phenomenon, schematically illustrated in Figure 1B, is further exacerbated by the presence of weaker ionic bonds that link network modifier elements such as alkaline cations. To combat this, the presence of a barrier coating on the internal surface of pharmaceutical vials has been explored as a potential solution to limit the interaction between the stored drug and the glass container. Pharmaceutical vials based on the above concept have already been commercialized. As an example, the product SCHOTT Type I plus involves a pure, 100−200-nm-thick SiO_2 coating, deposited by plasma impulse chemical vapor deposition (PICVD) on the internal surface of Type I glass.[16] The significant decrease in the drug-to-container interaction provides improved resistance against tests recommended by the European (EP) and the United States (USP) Pharmacopeias, and more specifically to the USP <660> chapter.[17] However, such coatings fail to resist satisfactorily against phosphate buffer solutions that approach the more aggressive USP <1660> chapter,[18] utilizing wet corrosion acceleration tests under extreme thermal and chemical conditions that replicate prolonged exposure of the glass surface to aggressive pharmaceutical substances.[19,20] Therefore, coating materials more resistant than silica need to be explored if they are to prevent the release of glass ions in the solution and withstand the severe USP <1660> tests. The water molecules can diffuse into the silica glass through void spaces in the structure, the diffusion pathway being primarily controlled by steric constrains imposed by the size of the voids and their interconnectivity. When the ring size opening is comparable in size with the water molecule (diameter of the water molecule is 0.28 nm), the only way for water to penetrate such a structure is to break open the rings via hydrolysis from a nucleophilic attack.[21] Water transport is then assured by hydrolysis−condensation reactions with Si−O bonds. In basic solutions, the solubility of silica enhances, and the hydrolysis reaction is favored compared to hydration. The topology of the network and the activation energy of the nucleophilic attack are then major parameters in the durability control of the coating.

As a response to this challenge, the present work investigates amorphous silicon oxynitride (SiO_xN_y) films based on the hypothesis that the partial replacement of divalent O^{2-} anions by trivalent N^{3-} anions results in a network of $Si-O_{4-x}-N_x$ tetrahedra, where Si atoms are occasionally bonded to one or more nitrogen atoms substituting oxygen, as schematized in Figure 1C. In this phase, the short-range disorder,[22] cross-linking,[23] and density[24] of the network are increased with regard to pure SiO_2. These changes, combined with the absence of crystalline grain boundaries, expectedly confer enhanced diffusion-barrier performance and chemical inertness to the SiO_xN_y coating, as was recently demonstrated.[25]

For such a material solution to be industrially transferable, coatings have to be applied conformally on the internal surface of pharmaceutical vials, cost effectively, and with deposition rates (DRs) matching the high production throughput in the order of thousand vials per hour. The thermally activated chemical vapor deposition (CVD) technique operating at atmospheric pressure meets these prerequisites in principle, the most severe constraints being achieving satisfactory deposition rates and, of course, overcoming development costs. However, before considering a potential transfer in industrial applications, which is beyond the scope of this work, a first technological bottleneck is that the deposition process should operate below 580 °C, the glass transition temperature of Type I vials, to ensure the dimensional integrity of the glass container. Applying silicon oxynitride coatings below this temperature is one of the major objectives of this work. This constraint has not been met in state-of-the-art thermal CVD chemistries targeting SiO_xN_y coatings, which typically operate in the 800−1200 °C range.[26] We have recently decreased this deposition temperature (T_d) range to ca. 600−650 °C thanks to the use of tris(dimethylsilyl)amine (TDMSA) as a single-source (Si, N) precursor without, however, meeting the abovementioned temperature target.[27] Further decrease of T_d can in principle be achieved by implementing trisilylamine-type chemistries with specifically engineered structures, for example, replacement of the methyl ligands on the silicon atoms by hydrogen and amine substituents. Moreover, limiting the number of stabilizing amine substituents confers higher reactivity compared to $SiH_x(NR_2)_{4-x}$ aminosilane-type chemistries with low x values. This is due to the greater reactivity of the Si−N bond when the molecule is not sterically hindered by multiple alkylamine chains. Additionally, the lower Si−H bond strength compared to Si−N and Si−C bonds also increases reactivity. Based on these observations, the present report implements *N*,*N*-bis(1-methylethyl)-*N*′,*N*′-disilyl-silanediamine (BMDSD, chemical structure illustrated in Figure 1C) as a single-source Si−N precursor. We demonstrate that this Air Liquide proprietary trisilylamine derivative with enhanced reactivity enables a SiO_xN_y thermal CVD below 580 °C.

We first investigate SiO_xN_y coatings on flat substrates and implement a large panel of characterization tools to reveal the dependence of the corrosion resistance, wettability, and mechanical properties on the nitrogen content, chemical bonding state, and nanostructure of the films. We then study their structure for variable nitrogen contents by molecular dynamics (MD) models, commonly used to investigate amorphous materials and glass.[28−30] We finally apply such SiO_xN_y coatings on the internal surface of pharmaceutical vials with the aim to reveal the compliance of chemical release during particularly challenging leaching tests and demonstrate unprecedented performance when subjected to USP <1660> tests. These tests involve vial filling with solutions containing potassium chloride, citric acid, and glycine for pH values between 8 and 10, treated above 50 °C for a duration from 2 to 24 h. The qualification of the coatings' chemical performance according to these severe tests is the second major objective of this work. A large panel of tools have been applied to accurately characterize the chemical, structural, and microstructural properties of these innovative layers deposited at a low temperature from the BMDSD molecule. Molecular dynamics study reveals strong structural changes induced by nitrogen substitution in the network, resulting in improved mechanical properties and chemical durability. This work aims to demonstrate the CVD process efficiency to produce strong hydrolytic resistance silicon oxynitride coatings on glass surfaces, illustrated here in the pharmaceutical context but transferable to multiple applications of surface coating by adaptation of the deposition conditions.

■ MATERIALS AND METHODS

Deposition of SiO_xN_y Films on Si Wafers and Their Characterization

Depositions on Si (100) wafer coupons (Neyco, 32 × 24 mm^2) were performed in an in-house designed horizontal tubular CVD reactor, schematized in Figure S1 and detailed in refs 27,31. The reactor setup allowed the treatment of multiple samples in a row, placed deliberately in regions with distinct local temperatures (described in the Supporting Information, SI), as a means to extract kinetic information for the elucidation of the SiO_xN_y deposition mechanism. This also facilitated the identification of optimal experimental conditions that lead to the desired film properties in terms of composition, structure, and barrier performance. The operating pressure was kept constant at 97.3 kPa (730 Torr), and the input gas was composed of BMDSD (95%, Air Liquide) flowing at 2 standard cubic centimeters per minute (sccm), N_2 (99.9999%, Messer) at 4028 sccm, and O_2 (99.9995%, Messer) at variable flow rates. Figure 2 summarizes the investigated parametric deposition conditions for seven experiments with two variables, the O_2/BMDSD flow ratio and deposition temperature T_d, varying between 0 and 0.30, and between 550 and 650 °C, respectively.

Film thicknesses were measured using a Semilab SE-2000 Spectroscopic Ellipsometer (SE) operating at an incidence angle of 70° using a methodology detailed in Section 2.1 of the SI. Each sample was probed at five points along the vertical center line, as illustrated in Figure S2A. The SE data were fitted in the 250−1000 nm wavelength range using a two-component Bruggeman effective medium approximation (BEMA) model consisting of SiO_2 and Si_3N_4.

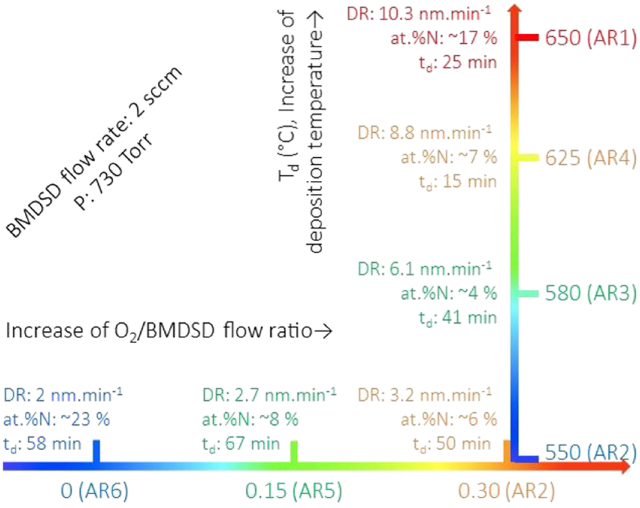

Figure 2. Experimental conditions of the performed BMDSD-O_2 parametric analysis tested in the tubular CVD reactor. The effect of the T_d is investigated through experiments AR1−AR4. The effect of the O_2/BMDSD flow ratio for a T_d of 550 °C is investigated through experiments AR2, AR5, and AR6. t_d: deposition time; DR: deposition rate.

It will be shown below that according to IR, X-ray photoelectron spectroscopy (XPS) analyses, and electron energy loss spectroscopy (EELS) results, Si- and C-rich arrangements are also incorporated in the films, albeit at small quantities. Then, a three-component BEMA model consisting of a homogeneous mixture of SiO_2, Si_3N_4 and amorphous C, or SiO_2, Si_3N_4, and amorphous Si (Figure S2B) also yields satisfactory fits (linear regression fit $R^2 > 0.99$). Since SE does not consider incorporation of hydrogen in the films, additional composition results considering the presence of H were obtained by Elastic Recoil Detection Analysis (ERDA), coupled with Rutherford Backscattering Spectroscopy (RBS) and Nuclear Reaction Analysis (NRA), schematically illustrated in Figure S2C. The applied conditions for this set of Ion Beam Analyses (IBA) are detailed in the SI. The values of the deposition rate and nitrogen content reported in Figures 2 and 4 were calculated from SE data and the SiO_2−Si_3N_4 two-component BEMA model completed by the H analysis deduced from ERDA measurements and C analysis deduced from NRA.

The corrosion resistance of the films was evaluated with the Buffered Oxide Etch (BOE) test, introduced in Section 2.2 of the SI and illustrated in Figure 3. The BOE test is usually applied for the etching of SiO_2, SiO_xN_y, and Si_3N_4 films.[32,33] Such etching solutions are used to indirectly assess the quality of silicate films based on their etching rate, which, according to Pliskin,[34] is relative to the density of the film. As a result, the etching rate is implicitly linked to network porosity, composition, and structure and can help concluding on these characteristics.

The chemical structure of the films was assessed in transmission mode by Fourier Transform Infrared Spectroscopy (FT-IR) in transmission mode on a Frontier FT-IR MIR/NIR instrument equipped with a custom-made substrate holder that allows rotation of the sample in relation to the incident beam. The vibration band deconvolution is executed as a qualitative approach considering information from the literature. Complementary chemical analysis was performed by X-ray Photoelectron Spectroscopy (XPS) in a ThermoFisher K-Alpha system. A low-energy flood gun delivering electrons and Ar^+ ions (<5 eV) to the sample surface was utilized in order to neutralize the surface charge during data acquisition. The acquisition process for both FT-IR and XPS and the postacquisition processing of the data are presented in Section 2.3 of the SI.

The wettability of the films was investigated by measuring their pure Water Contact Angle (WCA) with a GBX apparatus, using Young's equation.[35] The WCA values were captured using a CCD camera and the impact of surface roughness on WCA was evaluated by applying the model of Wenzel.[36]

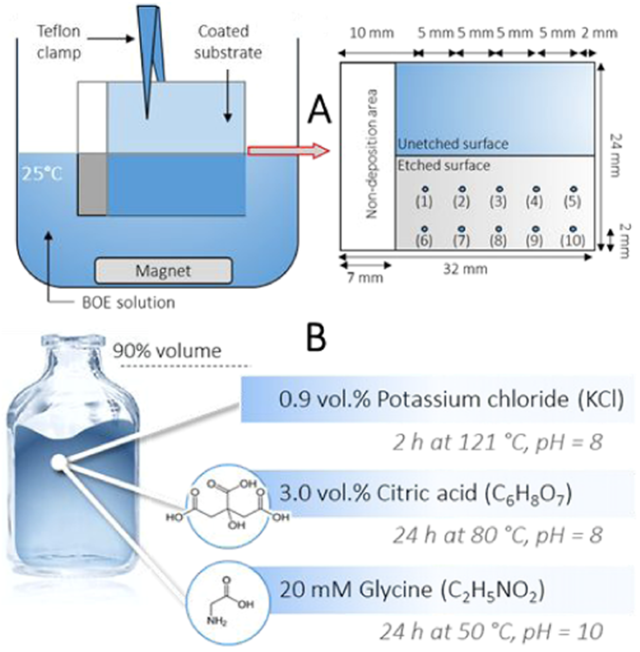

Figure 3. (A) BOE wet etching corrosion test. Schematic representation of the test configuration and locations probed by SE for the calculation of the etching rate. (B) USP <1660> tests. Schematic of the conditions defining the three test solutions (KCl, citric acid, and glycine), along with the duration, temperature, and pH.

The hardness and elastic modulus of the films were assessed by nanoindentation using an UltraNanoIndenter apparatus from CSM Instrument (Anton Paar) equipped with a Berkovich diamond indenter. Additionally, a depth-related analysis was performed by dynamic indentation tests where the load was varied sinusoidally with a 0.5 mN amplitude in the range of 7−40 mN. The intrinsic film properties were evaluated by subtracting the substrate contribution through the application of the Song−Phar model as described in ref 37. Dynamic indentation associated with models can accurately evaluate films with an expanded range of thickness, with a 50 nm thickness threshold. The evaluated oxynitride film thicknesses are in the 80−260 nm range. An additional experiment AR7 is conducted in the same conditions as AR1 for 80 min to obtain thicker SiO_xN_y films of 824 nm for the method validation. The adhesion of the SiO_xN_y films on Si substrates was assessed through nanoscratch using a Nanoscratch Tester from CSM Instrument (Anton Paar). Penetration, residual depths, and track images obtained with optical microscopy (Nanoscratch CSM) were used to analyze the results and determine the critical normal loads corresponding to coating adhesive failures. The critical load of delamination CL3, which is the normal force at which a film undergoing a nanoscratch test starts to delaminate from the substrate, was measured from the mean of three measurements repeated in different locations on the film. The wettability and mechanical tests are detailed in Section 2.4 of the SI.

High-resolution micrographs of the SiO_xN_y films and corresponding Energy Dispersive Spectroscopy (EDS) elemental information were acquired using a JEOL ARM200CF (JEOL Ltd.) Transmission Electron Microscope (TEM) operating at 80 kV. The instrument was equipped with double spherical aberration correctors and fitted with a JEOL SDD CENTURIO EDS system. A 0.13 nm probe size was used for EDS analysis. Before analysis, the cross section of the films was prepared by a Focused on Beam (FIB) technique using Ga^+ ions in a FEI HELIOS 600i instrument. TEM analysis was performed as soon as possible after FIB preparation to minimize contamination.

Deposition of SiO_xN_y Coatings on Vials and Their Characterization

Following the tuning of the deposition process and structural and functional characteristics of the films, deposition of SiO_xN_y coatings on the internal surface of Type I borosilicate pharmaceutical vials was carried out in a dedicated CVD setup, described in detail in ref 5,38 and schematized in Figure S8A. Vaporized BMDSD was supplied at 1 sccm with 2221 sccm of N_2 directed to the vial through a stainless steel (SS) nozzle located right above it. An inductively heated SS cylinder was positioned at the exterior of the quartz tube. Depositions were performed at 730 Torr and 550 °C nominal T_d corresponding to a temperature profile along the vial illustrated in Figure S5B. Deposition duration of 20 min resulted in a mean value of 4.51 mg of deposited SiO_xN_y mass, corresponding to 104 nm of average thickness of the film, assuming uniform deposition on all surfaces, excluding the exterior base surface.

The thickness and morphology of films deposited on vials were evaluated by SEM in an FEI Quanta450 (Bruker) instrument equipped with an EDX detector. Fragments of the vials were metallized with Ag by cathodic sputtering at reduced pressure for 30 s with a HHV Scancoat Six metallizer (Edwards). The observation conditions are detailed in Section 3.2 of the SI.

The screening strategy used for accelerated long-term suitability study of the coated vials was based on the USP <1660> tests. The testing methods recommended in the USP <1660> chapter are normally used for assessing delamination propensity but have also been adopted to test chemical durability in the long term. They are commonly applied as a comparative method to evaluate the suitability of various vial compositions prior to packaging. USP <1660> tests were performed with three different stress-test solutions, in an attempt to screen for multiple potential application cases. In particular, the tests were carried out using sodium chloride (KCl), glycine ($C_2H_5NO_2$), and citric acid ($C_6H_8O_7$) in conditions that are schematically illustrated in Figure 3B and detailed in Section 3.3 of the SI. Each test was carried out on three coated and three uncoated vials. Prior to testing, each vial is rinsed three times with water for pharmaceutical use (WPU). Then, it is filled to 90% of its maximum volume capacity with the respective solution and subjected to autoclave sterilization cycle according to the details for each test shown in Figure 3B. At the end of the autoclave cycle, the solution is acidified by adding 2% by volume of nitric acid (HNO_3, 65 m.%, SUPRAPUR Merck) to limit the precipitation of certain elements. The concentration of the extracted elements was determined with an Inductively Coupled Plasma Optical Emission Spectroscopy (ICP-OES) spectrometer (Optima 7300 DV, PerkinElmer), and the efficiency of the coating was assessed as the percentile difference of extractables concentration with respect to the extractables probed for uncoated vials. Normalized mass loss (NL_i) and equivalent thickness (ETh_i) of altered glass for i chemical element and referred to the bare borosilicate glass vial composition, have also been calculated in Section 3.3 of the SI.

Molecular Dynamics

The simulated bulk glass structures were generated with rigid ion potentials, developed by Unuma et al.,[39] using DL_POLY 4 package.[40] The box density (i.e., the volume) was kept constant during all simulations and approximated to a linear evolution between SiO_2 and Si_3N_4 (Table 1). Initial random structures (approximately 300 atoms in a cubic simulation box of an approximate length of 16 Å) were first equilibrated by a 100 ps NVT (atomic number, volume, temperature) run at a high temperature (3500 K), followed by quenching at a rate of 2.5 K·ps^{-1} from 3500 to 300 K in order to mimic the "melt-quench" technique. We studied four compositions in the SiO_2−Si_3N_4 system: 0, 2, 5, and 12 atom % N, named N0, N2, N5, and N12, respectively. The compositions and density of each model are reported in Table 1. For each composition, three structures were created to increase the statistics. Atomic positions of Molecular Dynamics (MD) models were optimized by Density Functional Theory (DFT) calculations using the CASTEP package[41] in order to correct defects due to imperfect empirical potentials. All computations were performed using the GGA PBE functional[42] and ultrasoft pseudopotentials (Materials Studio 7.0) generated "on-the-fly".[43] Geometrical features were calculated from the three different models for each nitrogen content in order to characterize the structural effects of nitrogen incorporation in the coating. Structures were analyzed using a custom python code. Atoms were clustered as a function of their speciation (i.e., coordination number, chemical bondings, etc.), calculating property distributions for each speciation. The cutoff radius used to perform structural analyses was set to 2.0 Å for Si−O and Si−N, corresponding to the first minimum of the partial distribution function.

Table 1. Molecular Dynamics Models[a]

name	N (Si)	N (O)	N (N)	density	box length (Å)
N0	100	200	0	2.200	16.503
N2	104	196	8	2.226	16.623
N5	108	192	16	2.267	16.667
N12	120	180	40	2.374	16.835

[a] Atomic composition, density, and box length for each model.

RESULTS AND DISCUSSION

Deposition on Si Coupons: Parametric Analysis

A parametric analysis studying deposition at four different T_d, namely, 550, 580, 625, and 650 °C was conducted (runs AR1−AR4 in Figure 2). The evolution of the Deposition Rate (DR) and the N content of the films along the reactor were measured by SE and are presented in Figure 4. Figure 4A shows that for T_d 650 °C, deposition is initiated at around 510 °C with a local DR of 0.9 nm·min^{-1}. The maximum DR at this T_d is 10.3 nm·min^{-1}, reached at ca. 635 °C. As T_d decreases, so does the global DR profile of each experiment, with the corresponding maximum DR values measuring 8.8, 6.1, and 3.2 nm·min^{-1} for 625, 580, and 550 °C. This behavior is expected for thermally activated processes. Additionally, it is noted that the maximum DR is observed closer to the inlet for higher T_d, which is explained by the offset between the thermal profiles. Faster heating of the gas phase at higher T_d leads to increased activation of the gas phase and surface reactions. Beyond the maximum DR, the film formation rate decreases for all experiments due to the consumption of one or multiple reactants in the gas phase.

Figure 4B reveals that for T_d = 650 °C, nitrogen is first encountered beyond 0.15 m from the inlet, corresponding to a local temperature of ca. 520 °C. Nitrogen incorporation is initiated further inside the reactor for the lower T_d as a result of the aforementioned thermal profile offset and the slower thermal activation of the gas phase. The nitrogen content of the films increases continuously. Deposition at T_d lower than 650 °C results in a decrease in nitrogen incorporation, with maximum values of approximately 6.9, 4.1, and 6.4 atom % N noted for T_d 625, 580, and 550 °C, respectively. Interestingly, most of the values for 580 and 550 °C overlap, even though clear differences in their respective DRs were shown in Figure 4A. This can indicate that at 550 and 580 °C, deposition and Si−N incorporation proceed through the same intermediate species. Above 580 °C, and especially at 650 °C, the deposition mechanism appears to be changing due to BMDSD decomposition, with deposition being carried out by multiple intermediate species that feature higher N:Si atomic ratios. This first parametric analysis illustrates the ability of the BMDSD precursor to successfully lead to SiO_xN_y deposition

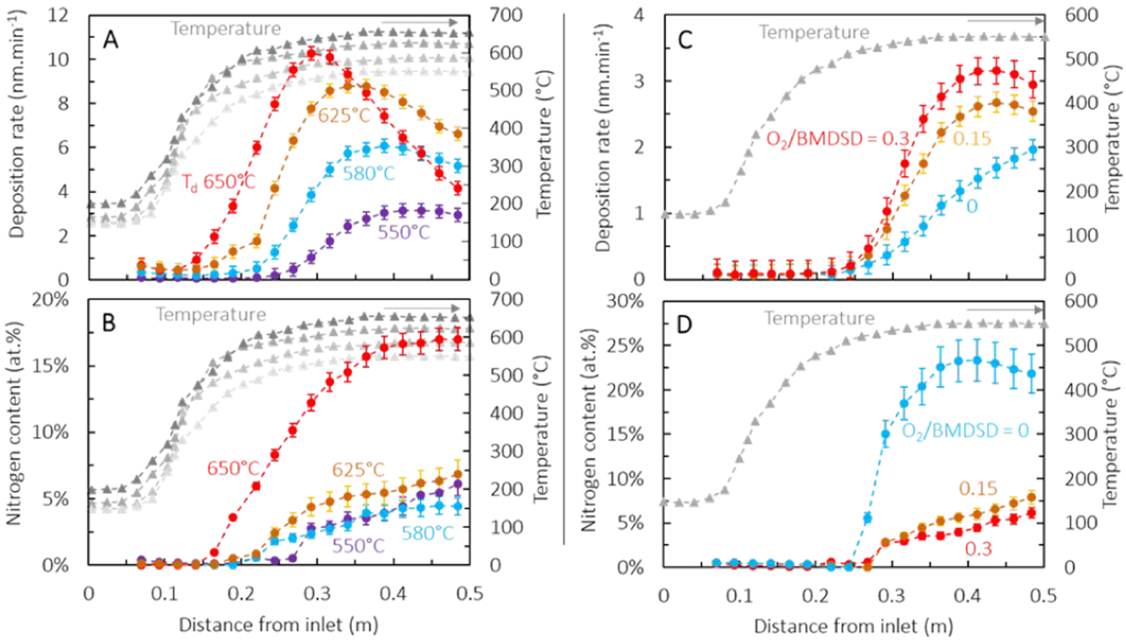

Figure 4. Parametric analysis of SiO_xN_y deposition. (A) Deposition rate and (B) nitrogen content in SiO_xN_y films produced for various T_d, at a 0.3 O_2/BMDSD flow ratio. The temperature profiles in the reactor are shown as gray data, with the lightest to the darkest corresponding to the lowest up to the highest T_d. (C) Deposition rate and (D) nitrogen content for SiO_xN_y films produced for variable O_2/BMDSD flow ratios, at T_d 550 °C. The temperature profile of T_d 550 °C is shown in the gray data. All four diagrams are presented as a function of the distance from the inlet; i.e., the position of each Si coupon.

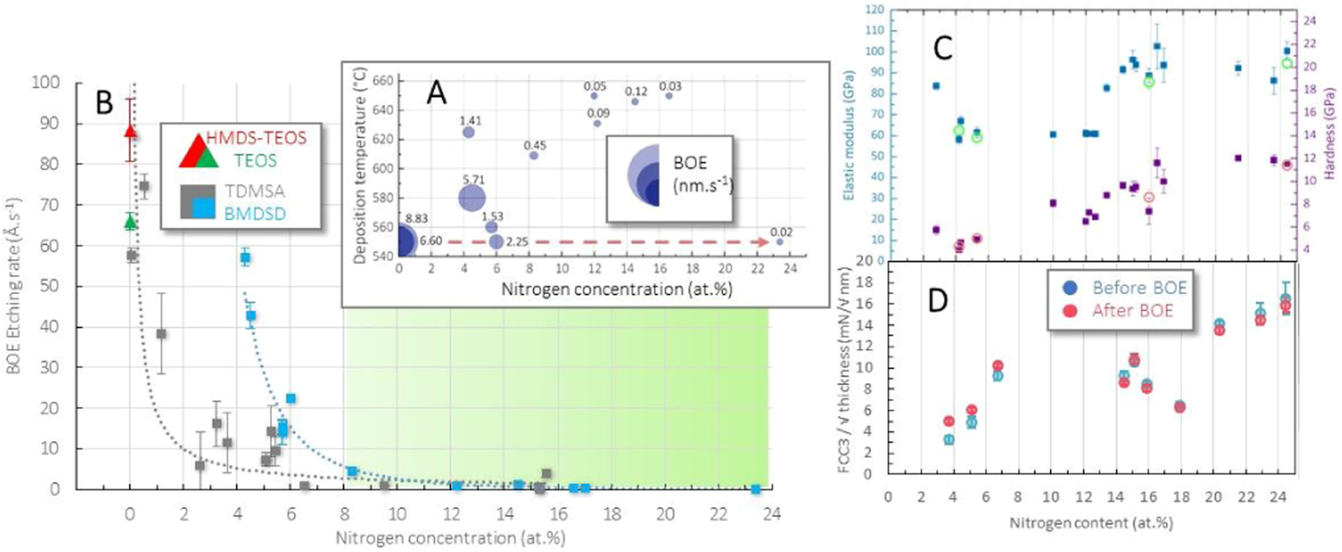

Figure 5. Functional properties of SiO_xN_y films. (A) BOE rate as a function of the nitrogen content and T_d. (B) BOE etching rate of SiO_xN_y from BMDSD (light blue squares), TDMSA[27] (gray squares), and SiO_2 and SiO_x films processed at 550 °C from TEOS[13] (green triangle) and HMDS-TEOS[15] (red triangle), respectively. Power trend lines were added for visual aid. (C) Elastic modulus (blue squares) and hardness (purple squares). Red and green open circles refer to values after BOE. (D) Critical force of delamination for SiO_xN_y films from BMDSD before and after BOE. Films in panels (C and D) were processed at T_d 550 °C.

featuring multiple advantages. First, high DRs of up to 10.3 nm·min^{-1} are noted. More importantly, deposition at temperatures as low as 510 °C is achieved with successful nitrogen incorporation at 520 °C and above. This feature is seminal for deposition of SiO_xN_y coatings at conditions that are compatible with the glass transition temperature of the Type I pharmaceutical vials and potentially for complementary applications involving deposition on other thermosensitive substrates by thermal CVD.

Following the achievement of SiO_xN_y deposition at temperatures lower than 600 °C, a second parametric analysis based on the O_2/BMDSD flow ratio at a constant T_d 550 °C was executed (runs AR2, AR5, and AR6 in Figure 2). The BMDSD flow rate was kept constant at 2 sccm, while the O_2 flow rate was varied in order to give 0.0, 0.15, and 0.3 O_2/BMDSD flow ratios. The DR and nitrogen incorporation results obtained from this parametric analysis are presented in the diagrams of Figure 4C,D. From Figure 4C, it is observed that a higher O_2 flow rate increases the overall DR of the

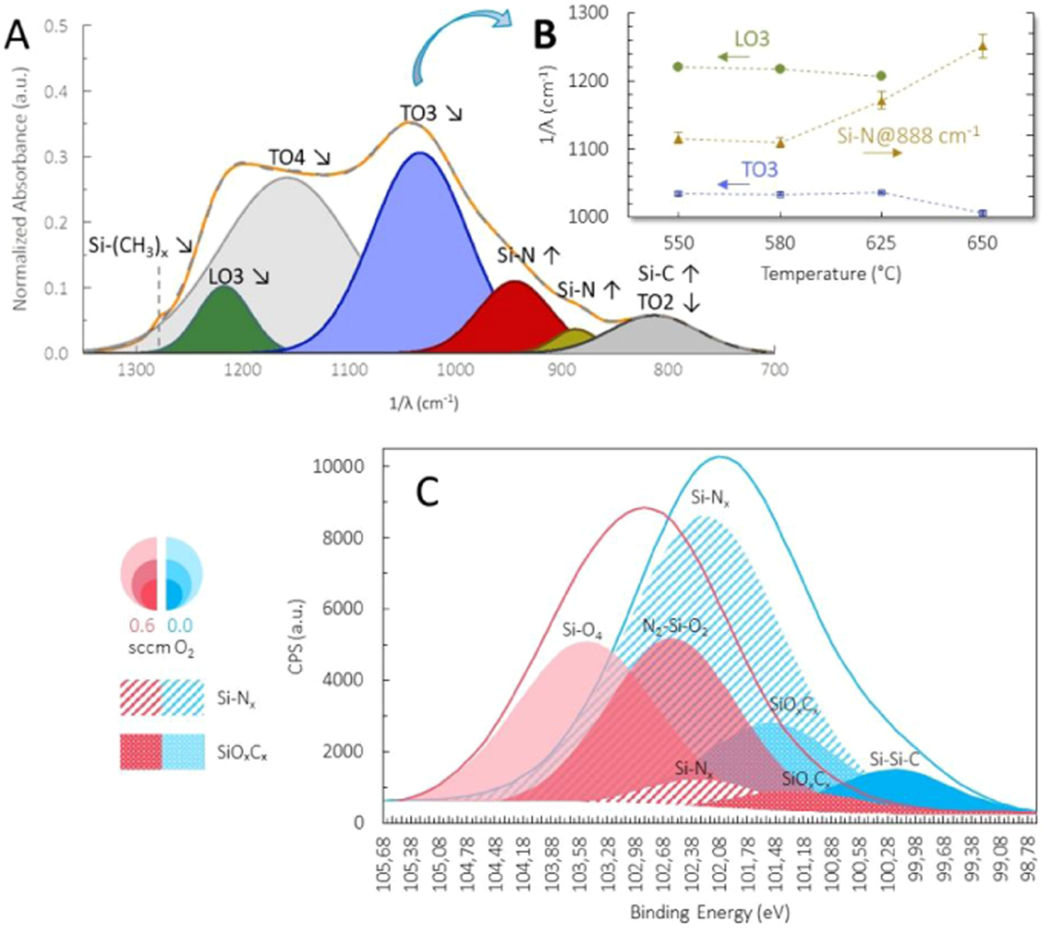

Figure 6. Structural and microscopic characteristics of SiO_xN_y films. (A) FT-IR fingerprint domain, with deconvolution of overlapping absorptions for a film processed at 625 °C at 0.3 O_2/BMDSD ratio. Trends with increasing T_d: shifts are indicated by →← and changes in intensity by ↓↑ arrows. (B) Peak position in wave numbers for LO3, TO3, and Si−N bands as a function of T_d at 0.3 O_2/BMDSD ratio. (C) XPS Si 2p deconvolution analysis for two SiO_xN_y samples processed at 650 °C with 0.3 O_2/BMDSD, and 550 °C with 0.0 O_2/BMDSD ratios.

process. In the absence of O_2, a maximum DR of 2.0 nm·min^{-1} is noted. This value increases to 2.7 and 3.1 nm·min^{-1} for 0.15 and 0.3 nm O_2/BMDSD ratios, respectively, illustrating the deposition-promoting effect of O_2. Film formation is observed even in the absence of an O_2 supply (0 sccm flow rate), indicating that the BMDSD precursor can dissociate and lead to deposition on its own. The obtained SE spectra still fit to a SiO_2 + Si_3N_4 model, with IBA measurements also probing the small O content in the films of this run.

The effect of the O_2/BMDSD flow ratio on the nitrogen content is shown in Figure 4D. Nitrogen incorporation is observed for all experiments. Similar to the first parametric analysis, the maximum N content is noted on the last sample of each run (p6, Figure S1C), measuring 6.1 atom % N at 0.3 O_2/BMDSD ratio. This value increases to 7.9 and 21.9 atom % N for 0.15 and 0 O_2/BMDSD ratios, respectively. These results clearly illustrate the competitive behavior of the incorporation of O and N, with nitrogen incorporation increasing for lower O_2 inlet supply. Because of the continuous consumption of O_2 in the gas phase, a progressive increase in the N concentration is noted along the length of the reactor. However, at 0 flow rate, a bell curve for the nitrogen content is observed after 0.4 m from the reactor inlet. Given that the DR continues to increase beyond 0.4 m, it is speculated that film formation in this region proceeds through multiple species, each containing different atomic N:Si ratios. The consumption of a species with a high N:Si ratio along with the prevalence of a species with a lower N:Si ratio could explain the decrease in the nitrogen content and concomitant increase in DR.

Corrosion Resistance, Wettability, and Mechanical Properties

Figure 5A presents the BOE rate as a function of the N content and the T_d of the films. We observe that low T_d and N-free films [0 atom % N processed from other CVD routes, namely, tetraethoxysilane (TEOS)[14] and hexamethyldisilazane (HMDS)[15] chemistries] result in high BOE rates, in the order of 6−9 nm·s^{-1}, which compromises their durability and barrier performance. For 4.5 atom % N SiO_xN_y films, we notice that the increase in T_d from 580 to 625 °C results in a decrease in the BOE rate from 5.7 to 1.4 nm·s^{-1}, considering, however, that T_d above 580 °C undermines the dimensional integrity of the pharmaceutical vials. Increasing the N content at a fixed T_d of 550 °C (red dashed arrow) results in a significant decrease in the BOE rate, becoming almost null for 23.5 atom % N (AR6). The strong correlation between the BOE rate and N content is confirmed by the diagram in Figure 5B, considering results on a large panel of samples obtained from various CVD processes. For a moderate nitrogen content, an increase from 4 to 8 atom % N in the silicate network results in a sharp decrease in the BOE rate, from 6 to 0.5 nm·s^{-1}, before flattening to values lower than 0.1 nm·s^{-1} for a higher N

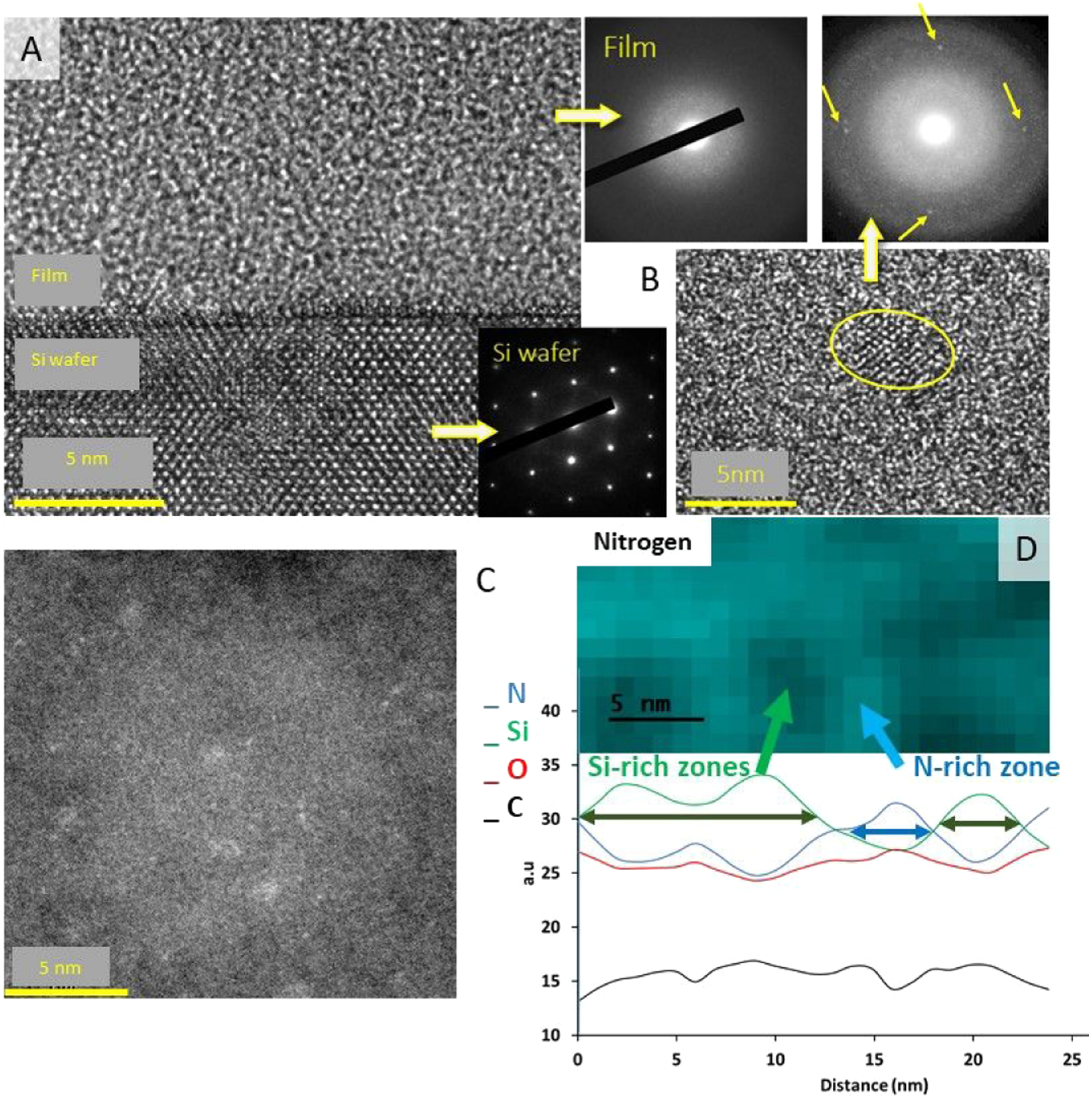

Figure 7. Film processed at 550 °C from a 0.0 O_2/BMDSD ratio. (A) High-Resolution Transmission Electron Microscopy (HRTEM) image of the film−substrate interface alongside their respective nanodiffractions. (B) Nanocrystallite isolated in the amorphous SiO_xN_y matrix and its nanodiffraction. (C) Scanning Transmission Electron Microscopy High Angle Annular Dark Field (STEM-HAADF) (Z-contrast) imaging, revealing brighter nanodomains in the film. (D) Nitrogen EELS map with the blue and green arrows pointing, respectively, at a N-rich and a N-poor nanodomain and locally extracted associated elementary profiles of Si, N, O, and C. The scales of both the map and profiles are the same.

content. The values for N-free films[14,15] and SiO_xN_y films from TDMSA at 600−650 °C[26] are also reported for comparison.

Water wettability measurements performed on various SiO_xN_y films are presented in Figure S7. WCAs measure between 53 and 63°. The films are expectedly hydrophilic and WCAs present a relatively flat evolution, with most values lying within the error bars. No particular influence of T_d could be evidenced. For T_d 550 °C, films with $N \leq 4$ atom % exhibit WCAs between 52.8 and 55.9°, while those with $N \geq 5.7$ atom % show WCAs in the range of 62.0−63.2°.

Figure 5C summarizes the Young's modulus and hardness and their evolution as a function of the N content of the films. In the two cases, two distinct regimes are observed before and after 12 atom % N, with low and high values. Their values span from 48.0 ± 2.1 and 4.0 ± 0.1 GPa (low regime), respectively, to 93.6 ± 5.1 and 11.6 ± 0.2 GPa (high regime). This high regime (N content > 12 atom %) can be correlated to the extremely low values of etching rate (Figure 5B). The resistance to delamination before and after BOE was evaluated by measuring critical load 3 (CL3). As shown in Figure 5D, a significant increase in scratch resistance with nitrogen content is observed, and the film mechanical properties remain unaffected after the BOE solution.

Composition, Chemical Bonding State, and Nanostructure

The composition of films deposited at T_d 550 °C is shown in Figure S3, as determined by IBA. When deposited from BMDSD alone, the films are composed of 45.1 atom % Si and 12.4 atom % O, the latter being attributed to the leveraging residual H_2O from the sample and process chamber.[24] The significant substoichiometry in O is compensated by a strong N content, namely, 23.7 atom % N, while C and H remain at levels of 8.0 and 10.8 atom %, respectively. Increasing the O_2/BMDSD ratio from 0 to 0.15 and then to 0.3 results in an increase in O and a decrease in N, illustrating, as already mentioned, the competitive incorporation of the two elements.

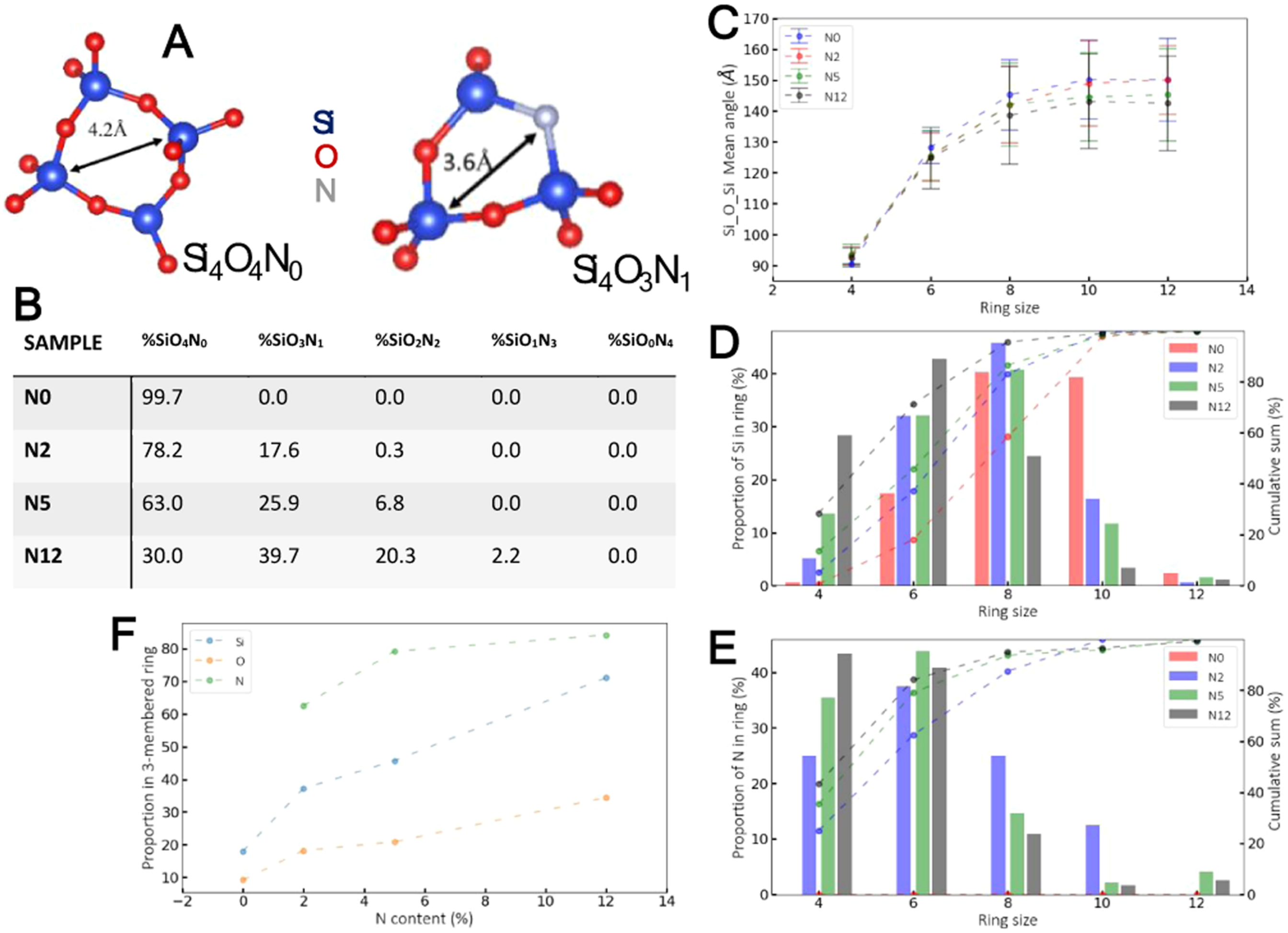

SAMPLE	%SiO_4N_0	%SiO_3N_1	%SiO_2N_2	%SiO_1N_3	%SiO_0N_4
N0	99.7	0.0	0.0	0.0	0.0
N2	78.2	17.6	0.3	0.0	0.0
N5	63.0	25.9	6.8	0.0	0.0
N12	30.0	39.7	20.3	2.2	0.0

Figure 8. Molecular dynamics simulation of an amorphous SiO_xN_y network. (A) Example of superstructural units extracted from MD models. The distances illustrate the diameters of the rings. (B) Proportion of $Si-O_{4-x}-N_x$ in all models for each composition. The presence of defects does not allow each row to sum to 100%, since only tetrahedral silicon is considered. (C) Evolution of the Si−O−Si mean bond angles as a function of the ring size. Ring size distribution and the associated cumulative sum, (D) for Si atoms and (E) N atoms. (F) Percentage of atoms involved in three-membered rings as a function of the N content.

Comparing the N content determined by IBA and that deduced by the SE model (Figure 4), apart from the value at the 0 O_2/BMDSD ratio, the N contents are rather underestimated by the SE model as discussed in the SI. Thermal treatments in NO and NO_2 are in progress to study the conditions of carbon and hydrogen disposal from the network.

The overall change in composition from N-rich to O-rich decreases the refractive index (RI, at λ=600 nm, Figure S3) from 2.0775 to 1.5251, approaching the RI value of pure SiO_2 (≈1.4772).

Table S1 presents the list of the identified absorptions by FT-IR spectroscopy corresponding to the chemical bonding of the SiO_xN_y films. As an example, Figure 6A shows the fingerprint domain of a film processed at 625 °C from 0.3 O_2/BMDSD. Multiple overlapping absorptions are encountered. General trends are extracted with increasing T_d for experiments AR1−AR4, illustrated with arrows that indicate the shift of the peak position and its change in intensity. The Si−N stretching vibration is noted as a shoulder appearing at ca. 940 cm^{-1}.[44] The higher contents of nitrogen for films produced at higher T_d shown in Figure 4B are reflected in the FT-IR spectra through the decrease of the LO3 and TO3 intensities and the parallel increase of the Si−N absorptions, as detailed and discussed in Figure S4. By extension, this illustrates the decrease in the number of $Si-O_4$ tetrahedra and the appearance of tetrahedra in which at least one oxygen is substituted by nitrogen.

In addition to the above, we also note an absorption at approximately 890 cm^{-1}, consistently appearing as a small shoulder for all temperatures (Figure S4A). Tracing its evolution (Figure 6B) reveals that its intensity increases for higher T_d. In parallel, its position shifts from 888 to 864 cm^{-1} (not shown). This absorption has been associated with the asymmetric stretching of Si−N in Si−NH−Si groups or the Si−H wagging vibrational mode[45] and has been reported to shift by more than 50 cm^{-1}. According to Behrens et al.,[46] two SiO_xN_y structures are suggested. The Random Mixture Model (RMM) is identified by a mixture of randomly distributed SiO_2 and SiO_xN_y phases leading macroscopically to an amorphous SiO_xN_y. Alternatively, the Random Binding Model (RBM) is encountered, where five different tetrahedral configurations of $Si-O_{4-x}-N_x$, with $x = 0-4$,[46,47] result in a homogeneous O−Si−N network. Multiple authors correlate the appearance of the aforementioned asymmetric stretching Si−N absorption to Si_3N_4 and, by extension, to the RMM configuration.[48]

Table 2. Proportion, in Percentage for Each Atom, of Coordination Numbers in Parentheses Calculated from Structural Models

models	O[1]	O[2]	O[3]	Si[3]	Si[4]	Si[5]	N[2]	N[3]	N[4]
N0	0.00	99.83	0.17	0.00	99.67	0.33	0.00	0.00	0.00
N2	0.34	98.13	1.53	1.28	96.80	1.92	20.83	79.17	0.00
N5	0.52	97.74	1.74	1.85	96.30	1.85	14.58	85.42	0.00
N12	0.56	96.30	3.14	3.61	92.50	3.89	10.83	89.17	0.00

In parallel, Figure 6C presents the deconvoluted XPS Si 2p spectra for two SiO_xN_y samples processed at the two extremes of the tested conditions (650 °C with 0.3 O_2/BMDSD, and 550 °C with 0.0 O_2/BMDSD). For high T_d and O_2 supply in Figure 6C, the Si 2p spectrum is deconvoluted into Si−(O)$_4$, N−Si−O, Si−N$_x$, and SiO_xC_x ($x \approx 2$), with binding energies of 103.5, 102.58, 102.3, and 101.28 eV, respectively. The tetrahedral configuration of Si−(O)$_4$ is matched with that of N_2−Si−O_2 in intensity, the latter being the primary binding state of the incorporated nitrogen. For low T_d and O_2 supply, however, Si−O_4 and N_2−Si−O_2 binding states disappear, which is well-coherent with the decreased O content revealed by IBA, and the decrease in LO3, TO3, and TO2 vibrations revealed by FT-IR. Instead, the mixed environment of Si is largely dominated by N and secondary by C and O, similar to the FT-IR spectral evolution. Table S2 summarizes the bonding states and energies of Si 2p, C 1s, N 1s, and O 1s spectra with the corresponding atomic concentrations for the experiment at 550 °C with 0.0 O_2/BMDSD. The strong Si−N$_x$ intensity in the XPS spectra correlates well with the increase in the asymmetric stretching Si−N absorption, hinting that higher incorporation of nitrogen induces a structural inhomogeneity resembling RMM networks. The appearance of the Si−Si−C binding state is also noted, giving rise to Si-rich zones as will be discussed in Figure 7A−D. Additional spectra are shown in Figure S5 for Si 2p, N 1s, and C 1s environments under varying deposition temperatures at a 0.3 O_2/BMDSD flow ratio, and under varying O_2/BMDSD flow ratio for T_d 550 °C. Table S3 summarizes the qualitative trends. It appears that Si−O and Si−N bonds coexist under the experimental conditions. However, for lower nitrogen content, the mixed O−N−Si−O contribution is preferred in agreement with the RBM model, while for higher nitrogen content, Si−N$_x$, Si−O$_x$−C$_x$, and O−N−Si$_2$ contributions are revealed, showing separated Si−N and Si−O networks and a global structure that evolves according to the RMM model, in agreement with the structural and mechanical results.

The nanostructure of a 65 nm-thick film AR6 with 22.6 atom % N, processed at 550 °C and 0.0 O_2/BMDSD flow ratio, was characterized by Transmission Electron Microscopy (TEM) (Figure 7A), showing perfect cohesion without porosity or defects. Nanodiffraction analysis (Figure 7B) illustrates an amorphous state. However, a few nanocrystallites can be observed locally in the film. The limited number of points on the corresponding nanodiffractions did not allow the identification of their crystalline nature. In the Z-contrast imaging mode of Scanning Transmission Electron Microscopy High Angle Annular Dark Field (STEM-HAADF, Figure 7C), we observe nanometer-scale brighter domains corresponding to higher density or local enrichment in a heavier element. Elementary maps acquired by Electron Energy Loss Spectroscopy (EELS) spectrum imaging have shown nanodomains enriched in Si or N. A profile through these maps (Figure 7D) confirms these local variations and reveals slight variations in the O and C contents.

Structural Investigations Using MD Simulation and DFT Calculations

The generated networks for the four N0, N2, N5, and N12 investigated models are entirely polymerized, composed of corner-sharing Si−O$_{4-x}$−N$_x$ tetrahedra and arranged in superstructural ring units of various sizes, examples of which are shown in Figure 8A. Oxygen atoms bonded to two silicon atoms coexist with nitrogen atoms bonded to three silicon atoms, independent of the nitrogen content for these low and medium contents, in agreement with the FT-IR and XPS results. Table 2 presents the percentage of coordination numbers for Si, N, and O atoms, calculated from N0, N2, N5, and N12 models. The majority of atoms are 2-, 3-, and 4-fold coordinated for O, N, and Si atoms, respectively; a few percent are over- or undercoordinated. Although these coordinations are not expected, they remain in the minority, indicating on average good quality of the models. These coordination defects increase with the nitrogen content from N0 to N12. Feuston et al.[49] reported a strong physical association between the three-membered ring and three-coordinated oxygen. This study could explain the emergence of three-coordinated oxygen in our models as the proportion of the three-membered ring also increases with the nitrogen content (discussed later). In another context, undercoordinated Si was already reported in the literature, with MD simulations strictly dedicated to amorphous silica surfaces. Mahadevan et al.[30] show the correlation between some of these defects, which get a structural meaning, and the chemical attack by water. In particular, undercoordinated Si′ at the surface of the glass could react favorably with hydrated species and enhance the reactivity of the surface. Increase of such defects with nitrogen content could be correlated to the chemical local variations and nanocrystallites observed by TEM-EELS.

The table in Figure 8B summarizes the statistical distribution of O and N atoms in the tetrahedra forming the glass network. No SiO_0N_4 unit is observed in the explored nitrogen range. The occurrence of SiO_3N_1 increases with nitrogen incorporation and becomes the predominant configuration at 12 atom % N. These results confirm the RBM description of the network for moderate N content.

As a complement, the evolution of the mean length of the Si−O and Si−N bonds as a function of the ring size is illustrated in Figure S6A,B for the four compositions. Expectedly, the mean bond length of Si−O is shorter than that of Si−N (1.63 vs 1.74 Å[50]). A weak decrease is observed in the Si−O bond length with increasing ring size and the nitrogen content in the silica network. The Si−N bond length is even less affected by the nitrogen content, indicating that the increase of structural constraints with higher nitrogen incorporation in the network does not induce any significant modification in the distribution of the bond lengths between silicon and the linkers. This observation shows that the bond

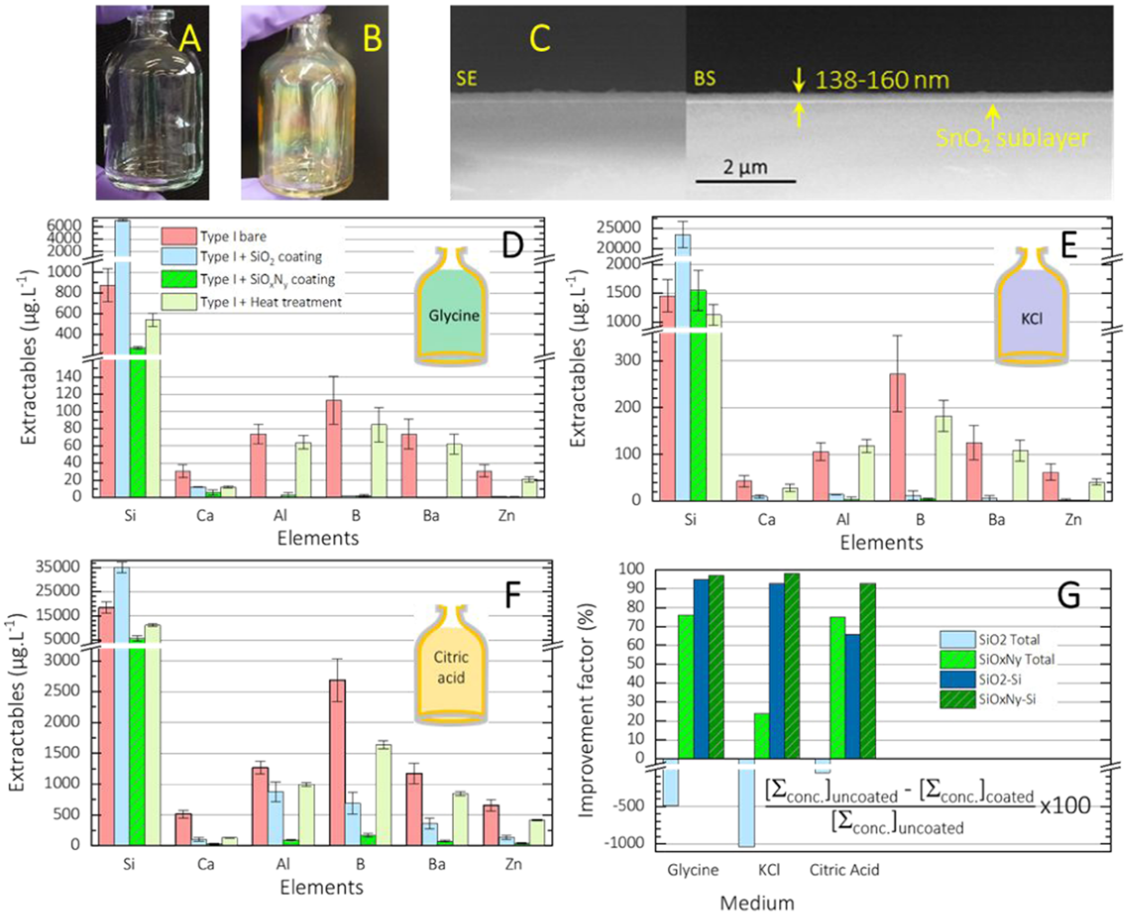

Figure 9. Coated vials and USP <1660> performance. Photographs of (A) as-received and (B) SiO_xN_y-coated vials. (C) Cross-sectional SEM micrograph in secondary (SE) and backscattered (BS) electrons of the exterior of the treated vial revealing a 138−160 nm thick film, depending on the probed zone, in agreement with the iridescence observed in panel (B). (D−F) Results following the USP <1660> chapter for bare (pink bars), SiO_xN_y-coated (green hatched), SiO_2-coated (light blue), and vials subjected to thermal treatment mimicking the SiO_xN_y deposition conditions (light green). The schematized vial indicates the solution used for the test: (D) glycine, (E) potassium chloride, and (F) citric acid. (G) Histogram summarizing the IF values for SiO_2 and SiO_xN_y-coated vials considering all elements (light blue and hatched green bars, respectively) and all elements except Si (dark blue and hatched dark green bars, respectively). The formula for the IF calculation is also reported.

length could allow only a small degree of freedom to the constrained glass network.

The histograms of Figures 8D,E and S6E show the percentage in rings of different sizes of Si, N, and O atoms, respectively, for the four compositions investigated. For all three atoms, we observe the distribution shift toward the smallest rings with nitrogen substitution. Indeed, addition of nitrogen in the structure results in the decrease in the size of the rings and in the increased concentration of nitrogen in the smallest rings (Figure 8E). Figure 8D shows that the model predicts a predominant ring size between 8 and 10 atoms (four-, five-membered ring) in N0 instead of 12 determined experimentally,[51,52] probably due to the small box size. Du et al. succeeded in reproducing the experimental ring size distribution but they developed their model in a box size of 30 Å compared to 16 Å in our case constrained by the DFT calculation time.[53]

The evolution of the mean bond angle value for Si−O−Si, Si−N−Si, and Si−L−Si configurations as a function of the ring size is shown in Figures 8C and S6C,D, respectively. Si−L−Si corresponds to the angle between two silicon atoms linked by a linker (N or O). While the Si−N−Si angle (Figure S6C) is moderately impacted with only a weak variation from 118.1 ± 11.9° for N2 to 117.0 ± 18.1° for N12, the impact on the Si−O−Si angle (Figure 8C) is more pronounced, and its value is reduced from 147.0 ± 14.0° in N0 to 132.6 ± 19.5° in N12. These distinct behaviors between Si−O−Si and Si−N−Si are attributed to the coordination difference between oxygen and nitrogen that much more constrained the Si−N−Si around 120°. Substitution of oxygen by nitrogen quickly results in the decrease of the mean Si−O−Si intertetrahedral angles and their standard deviation, reflecting the network topology loss of degree of freedom induced by the three-membered rings (bond angles in a three-membered ring should be around 120°). These results are perfectly in agreement with Murakami et al.'s ab initio calculations that show that in the silica glass, SiO_4 tetrahedra are bonded to each other with a flexible potential at the brindging oxygen, while the substitution of nitrogen for the bridging oxygen causes the $Si(O,N)_4$ tetrahedra to be fixed tightly at the bridging nitrogen atom.[54] This inflexible nature is attributed to Si−N−Si bonding and the additional effect of N coordination by three Si atoms. This property explains the higher elastic modulus observed with nitrogen substitution (Figure 5).

The ring size distribution exhibits significant changes in the intermediate range order between N0 and N12. Figure 8F shows a noteworthy increase in the proportion of atoms in three-membered rings, involving up to 70% silicon and 85%

nitrogen atoms for N12. Such small rings are particularly constrained units geometrically given the mean intertetrahedral angle of 120°. The addition of nitrogen reduces the size of the rings, resulting in a significant modification of the intertetrahedral bond angles (Figure S6F). Admittedly, rings larger than the considered superstructural units may still exist in the glass. These strong structural changes, when nitrogen content increases, could explain the evolution toward the RMM model for highest nitrogen contents (not explored by MD). The small diameter of three-membered rings (approximately 3.2−3.6 Å) renders diffusion of ions and hydrated species through the coating more difficult, regarding steric constraints. The glass topology and, in particular, the ring size distribution have an impact on the hydrated species' ability to penetrate the glass by diffusion. In this context, a threshold at around 7 Å separates two diffusion regimes, a liquid-state diffusion above the threshold with an apparent diffusion coefficient of the order of 10^{-9} $m^2 \cdot s^{-1}$, and a solid-state diffusion below, with an apparent diffusion coefficient lower than 10^{-15} $m^2 \cdot s^{-1}$.[8] Thanks to N substitution, the silicon oxynitride network evolves then into a more interconnected and compact network capable of slowing the hydration. As a result, and taking into account the higher covalence degree of the Si−N chemical bonds compared to Si−O,[54] which would reduce the rate of attack of the glass network by OH^- anions,[55] nitrogen substitution results in a more compact network with higher diffusion-barrier performance, hence higher resistance to hydrolysis and corrosion compared to pure silica films as shown by BOE tests in Figure 5A.

State-of-the-Art USP <1660> Performance of SiO_xN_y-Coated Vials

Photographs of pristine (Figure 9A) and SiO_xN_y-coated (Figure 9B) vials are presented in Figure 9, demonstrating the yellowish tint conferred by the coating due to the interference phenomena and iridescent effect. Probably some color centers as Si−Si defects contribute also to this tint, in accordance with the XPS results and EELS map, suggesting the presence of such defects for the highest nitrogen content. The cross-sectional micrograph of Figure 9C shows the coating formed on the external surface of the vial, typically covered with a thin tin oxide SnO_2 film that allows differentiating SiO_xN_y from the glass. The coating exhibits a thickness between 138 and 160 nm. The four surface SEM micrographs of Figure S9 summarize the morphology of the coating deposited on the interior surface at different positions of the vial. A continuous coating surface is observed, with the EDS spectrum containing a significant peak of N, in agreement with the 22.8 atom % N content of films deposited under the same conditions on flat surfaces, reported in previous sections. The film is surmounted by nodules at the shoulder, body, and heel. Their chemical analysis does not reveal noticeable differences from the underlying surface, and their formation is attributed to homogeneous, gas-phase side-reactions producing powder particles that are incorporated with the growing film.

The results of the USP <1660> tests are summarized in the three histograms of Figure 9, corresponding to the three test media, namely, glycine (Figure 9D), potassium chloride (Figure 9E), and citric acid (9F) and showing the concentration of leached glass-constituent elements, referred to as "extractables". The conversion of the extractables' concentration to NL_i has been calculated in the SI. Some NL_i and ETh_i values are given here in parentheses for comparison purposes. For all three media, the SiO_xN_y-coated vials obtained with T_d at 550 °C for 0.00 O_2/BMDSD ratio (bright green hatched bars) show noticeable Si extractables and extremely low to very low values (quantification limits are indicated in Table S4) for all other elements. For the glycine and citric acid tests, the uncoated vials (pink bars) show 3-fold higher concentrations of Si extractables compared to the coated vials. For KCl, the Si values of the SiO_xN_y coating are comparable to the uncoated vials, but concentrations of small cations such as B are significantly lower, i.e., 5 ± 2 $\mu g \cdot L^{-1}$ [0.6 $mg \cdot m^{-2}$ and 0.3 nm] compared to 272 ± 81 $\mu g \cdot L^{-1}$ [30.5 $mg \cdot m^{-2}$ and 13.7 nm] for uncoated vials.

The question is now raised of how the SiO_xN_y coating compares to a SiO_2 one for a comparable deposition temperature and film thickness. To answer this question, we deposited silica coatings from tetraethoxysilane (TEOS) and oxygen, as reported previously.[13] Figure 9 shows that their Si extractables (light blue bars) are systematically higher than those of both the SiO_xN_y coating and the bare vial, indicating the high sensibility to hydrolysis of the SiO_2 network even for an optimized silica coating[13−15] less resistant here to aggressive media than the bulk glass network, borosilicate network being considered as very durable.[8,10] Despite this weakness, the established barrier property of the SiO_2 coating results in a moderate decrease in the other extractables, exhibiting a convenient barrier to the diffusion of cations without sustaining an aggressive contact with the test solutions. In contrast, the SiO_xN_y coating is far more efficient and durable, assuring a very low diffusion of the hydrated species of the test solution and of the glass vial cations. Its efficiency is exemplified by the level of Al extractables in citric acid medium, namely, 874 ± 165 $\mu g \cdot L^{-1}$ for SiO_2 coating [143.8 $mg \cdot m^{-2}$ and 64.5 nm] and 90 ± 9 $\mu g \cdot L^{-1}$ for SiO_xN_y [14.8 $mg \cdot m^{-2}$ and 6.6 nm], an almost 10-fold decrease, compared to 1267 ± 101 $\mu g\ L^{-1}$ for the bare vial [208.4 $mg \cdot m^{-2}$ and 93.5 nm]. The performance of the SiO_xN_y coating also favorably compares with that of commercial SiO_2 coated vials, which, in identical USP <1660> recommended stress tests present 1−2 orders of magnitude higher concentration of Si extractables in the case of KCl and glycine tests (comparable in that of citric acid).[12] The authors also reported close to zero boron and aluminum extractables for such commercial vials; however, comparison with the present work is not possible due to a significantly higher limit of quantification (0.1 $mg \cdot L^{-1}$ therein, to be compared with less than 1 $\mu g \cdot L^{-1}$ in the present case).

By way of comparison, a large amount of NL_i data have been collected in the context of long-term silicate glass corrosion applied to nuclear glass study with many glass composition-dependent data.[8] An initial dissolution rate regime r_0 characterizes the first kinetic regime of silicate glass alteration in diluted solutions, and a residual alteration rate regime r_r of alteration takes place when a high concentration of dissolved silica enriched the solution and a passivating alteration layer is formed at the glass surface. These rates are calculated from NL_i measurements, generally estimated from boron concentration, considering as a tracer element. Then, at 90 °C and pH 9, the r_0 values are highly dependent on the glass composition with values in the range of 0.3−8.2 $g \cdot m^{-2} \cdot day^{-1}$ for nuclear glass,[8] when the r_r values stay in the range of 0.1−2 $mg \cdot m^{-2} \cdot day^{-1}$ regarding the experimental protocol. Even though these conditions are very far from the test protocols USP <1660>, we can observe that the order of magnitude for boron NL_i values of SiO_xN_y coating vials calculated here for a very short time is consistent with the residual rate range of nuclear glass, when for bare vials, the order of magnitude corresponds to the best values of r_0 retained for nuclear glass, as expected for the type I borosilicate glass.

Furthermore, deposition of SiO_xN_y occurs for 20 min. During this period, the vial is subjected to thermal treatment equivalent to T_d (550 °C). The question then arises as to whether the observed barrier performance is due to the coating, to the heat treatment of the vial, or to both. Indeed, heat treatment can improve the densification of the silicate network[13,14] and can also induce an interdiffusion zone between the glass and the coating that could act as an efficient barrier on its own.[5] To clarify this effect, we subjected bare Type I vials to a heat treatment reproducing the same thermal conditions that prevail during the application of the coating including the heating and cooling steps and subjected them to the exact same USP <1660> tests utilized for the coated vials. The results are illustrated as light green bars of Figure 9 and show an almost systematic decrease of the concentration of the cations extracted from the annealed vials compared to that from the as-received vials. However, this improvement is by far weaker than that conferred by the SiO_xN_y coating. Therefore, we conclude that the primary source of improved barrier performance is deposition of the SiO_xN_y coating itself. However, thermal treatment could potentially allow further enhancement of the barrier properties of the SiO_xN_y coating.

We quantify the comparative evolution of the leached cations by an improvement factor (IF), defined as the percentile relative change in the total element concentration in the solution conditioned in a coated vial, $[\Sigma_{concn}]_{coated}$, in relation to their concentration in the solution conditioned in an uncoated vial, $[\Sigma_{concn}]_{uncoated}$. The highest value of IF (100%) corresponds to complete barrier performance and the leached element content in the solution, lower than the quantification limits. The results are summarized in Figure 9G. In this histogram, SiO_2 and SiO_xN_y coatings are compared in light blue and hatched green bars, respectively, first considering the total amount of leached elements (Si+Ca+Al+B+Ba+Zn). We observe that the IF for the SiO_xN_y-coated vials is strongly positive, ranging from 24% for KCl to 75−76% for glycine and citric acid. In contrast, the IF for the SiO_2-coated vials is −1000, −490 and −51%, respectively, indicating that the total concentration of extractables for coated vials is higher than that of uncoated vials. To evaluate the pure barrier performance of the coatings, we determine their IF without considering the concentration of leached Si cations, which we hypothesize originates mainly from the coating itself. The results, reported by the dark blue (SiO_2 coating) and dark green (SiO_xN_y coating) bars, show positive and high IF for both, ranging from 66 to 95% for SiO_2 and from 93 to 98% for SiO_xN_y. The IF of the latter is systematically higher than that of the former. The obtained values for the SiO_xN_y coating reveal an almost complete diffusion-inhibition of the cations and confirm its exceptional barrier performance and strong chemical inertness against the standard test conditions. This breakthrough performance compared to SiO_2, combined with the achieved deposition of SiO_xN_y films at temperatures compatible with the glass container, establishes the demonstrated CVD process as a promising solution for sustainable packaging of future/sophisticated medicinal substances and other applications requiring an extreme inertia of glass.

■ CONCLUSIONS

The application of SiO_xN_y coatings on pharmaceutical borosilicate vials was made possible by an innovative, scalable CVD process involving the BMDSD precursor. The coated vials withstand the most aggressive accelerated aging tests of the USP <1660> chapter, for example, by preventing the diffusion of boron, a very mobile cation incriminated in the delamination mechanism, and silicon, representative of the glass network. N concentration as low as 5 atom % provides coatings with anticorrosion performance that surpasses state-of-the-art SiO_2 coatings. Refractive index, water contact angle, elastic modulus, hardness, and film chemical durability in basic media increase with increasing nitrogen incorporation. Structural characterizations and MD simulations show that such exceptional performances are attributed to the incorporation of N in substitution in the $Si-O_4$ amorphous network, resulting in the formation of covalent Si−N bonds and inflexible Si−N−Si bonding. Consequently, the size of the rings that compose the SiO_xN_y network decreases, and the chemical bond network is densified. The nitrogen-enriched amorphous network tends to become more chemically inert and compact, rendering diffusion of ions and hydrated species through the coating more difficult. CVD SiO_xN_y films with such breakthrough performance compared to SiO_2, and processed at moderate temperatures compatible with the glass container, are a promising solution for sustainable packaging of future medicinal substances, marking a significant step forward. By extension, the CVD processing at moderate temperature of such SiO_xN_y films with tunable composition and properties also paves the way for their implementation in other sectors that require chemically reinforced or functionalized glass, for example, to reduce the glass aging, daily glassware in the context of food contact materials, applications in polluted environment, antiweathering of soda-lime silicate glasses, and encapsulation layer of a device. Thermal treatments under suitable atmosphere have to be explored to optimize the coatings for a large panel of applications. In that case, the influence of glass composition and the surface nature, e.g., the tin side of float glass surfaces or SO_2 dealkalization, should be investigated.

■ ASSOCIATED CONTENT

Supporting Information

The Supporting Information is available free of charge at https://pubs.acs.org/doi/10.1021/acsaenm.3c00584.

> (1) SiO_xN_y coatings on Si wafers; (2) thin film characterization methods; (2.1) thickness and composition evaluation; (2.2) etching corrosion tests; (2.3) network structure and chemical bonding; (2.4) wettability, mechanical properties, and microscopy; (3) deposition of SiO_xN_y coatings in pharmaceutical vials; (3.1) CVD reactor setup; (3.2) vial samples and their characterization; (3.3) United States Pharmacopeia USP <1660> tests; and (4) references (PDF)

■ AUTHOR INFORMATION

Corresponding Author

Nadia Pellerin − *Conditions Extrêmes et Matériaux: Haute Température et Irradiation (CEMHTI), Orléans F-45100, France; Université d'Orléans, Orléans F-45100, France; CNRS, délégation Centre Limousin Poitou Charente, Orléans*

F-45100, France; orcid.org/0000-0002-9436-3480;
Email: nadia.pellerin@univ-orleans.fr

Authors

Konstantina Christina Topka – *Centre Interuniversitaire de Recherche et d'Ingénierie des Matériaux (CIRIMAT), Toulouse F-31062, France; Laboratoire de Génie Chimique (LGC), Toulouse F-31062, France; INP, Toulouse F-31400, France; Université Toulouse III, Toulouse F-31062, France; CNRS, délégation Occitanie Ouest du CNRS, Toulouse F-31062, France;* Present Address: Air Liquide Japan, Innovation Campus Tokyo, 2-2 Hikari-no-oka, Yokosuka-shi, Kanagawa 239-0847 Japan

Babacar Diallo – *Conditions Extrêmes et Matériaux: Haute Température et Irradiation (CEMHTI), Orléans F-45100, France; Université d'Orléans, Orléans F-45100, France; CNRS, délégation Centre Limousin Poitou Charente, Orléans F-45100, France;* orcid.org/0000-0003-1400-9463

Maxime Puyo – *Centre Interuniversitaire de Recherche et d'Ingénierie des Matériaux (CIRIMAT), Toulouse F-31062, France; INP, Toulouse F-31400, France; Université Toulouse III, Toulouse F-31062, France; CNRS, délégation Occitanie Ouest du CNRS, Toulouse F-31062, France*

Erwan Chesneau – *Conditions Extrêmes et Matériaux: Haute Température et Irradiation (CEMHTI), Orléans F-45100, France; Université d'Orléans, Orléans F-45100, France; CNRS, délégation Centre Limousin Poitou Charente, Orléans F-45100, France*

Farah Inoubli – *Conditions Extrêmes et Matériaux: Haute Température et Irradiation (CEMHTI), Orléans F-45100, France; Université d'Orléans, Orléans F-45100, France; CNRS, délégation Centre Limousin Poitou Charente, Orléans F-45100, France*

Simon Ponton – *Centre Interuniversitaire de Recherche et d'Ingénierie des Matériaux (CIRIMAT), Toulouse F-31062, France; Laboratoire de Génie Chimique (LGC), Toulouse F-31062, France; INP, Toulouse F-31400, France; Université Toulouse III, Toulouse F-31062, France; CNRS, délégation Occitanie Ouest du CNRS, Toulouse F-31062, France*

Cecile Genevois – *Conditions Extrêmes et Matériaux: Haute Température et Irradiation (CEMHTI), Orléans F-45100, France; Université d'Orléans, Orléans F-45100, France; CNRS, délégation Centre Limousin Poitou Charente, Orléans F-45100, France*

Diane Samelor – *Centre Interuniversitaire de Recherche et d'Ingénierie des Matériaux (CIRIMAT), Toulouse F-31062, France; INP, Toulouse F-31400, France; Université Toulouse III, Toulouse F-31062, France; CNRS, délégation Occitanie Ouest du CNRS, Toulouse F-31062, France;* orcid.org/0000-0003-3245-0658

Raphael Laloo – *Centre Interuniversitaire de Recherche et d'Ingénierie des Matériaux (CIRIMAT), Toulouse F-31062, France; INP, Toulouse F-31400, France; Université Toulouse III, Toulouse F-31062, France; CNRS, délégation Occitanie Ouest du CNRS, Toulouse F-31062, France*

Daniel Sadowski – *Centre Interuniversitaire de Recherche et d'Ingénierie des Matériaux (CIRIMAT), Toulouse F-31062, France; INP, Toulouse F-31400, France; Université Toulouse III, Toulouse F-31062, France; CNRS, délégation Occitanie Ouest du CNRS, Toulouse F-31062, France*

Cédric Charvillat – *Centre Interuniversitaire de Recherche et d'Ingénierie des Matériaux (CIRIMAT), Toulouse F-31062, France; INP, Toulouse F-31400, France; Université Toulouse III, Toulouse F-31062, France; CNRS, délégation Occitanie Ouest du CNRS, Toulouse F-31062, France*

Takashi Teramoto – *Air Liquide Japan, Innovation Campus Tokyo, Yokosuka-shi, Kanagawa 239-0847, Japan*

François Senocq – *Centre Interuniversitaire de Recherche et d'Ingénierie des Matériaux (CIRIMAT), Toulouse F-31062, France; INP, Toulouse F-31400, France; Université Toulouse III, Toulouse F-31062, France; CNRS, délégation Occitanie Ouest du CNRS, Toulouse F-31062, France*

Thierry Sauvage – *Conditions Extrêmes et Matériaux: Haute Température et Irradiation (CEMHTI), Orléans F-45100, France; Université d'Orléans, Orléans F-45100, France; CNRS, délégation Centre Limousin Poitou Charente, Orléans F-45100, France*

Hugues Vergnes – *Laboratoire de Génie Chimique (LGC), Toulouse F-31062, France; INP, Toulouse F-31400, France; Université Toulouse III, Toulouse F-31062, France; CNRS, délégation Occitanie Ouest du CNRS, Toulouse F-31062, France;* orcid.org/0000-0002-3511-5436

Marie-Joelle Menu – *Centre Interuniversitaire de Recherche et d'Ingénierie des Matériaux (CIRIMAT), Toulouse F-31062, France; INP, Toulouse F-31400, France; Université Toulouse III, Toulouse F-31062, France; CNRS, délégation Occitanie Ouest du CNRS, Toulouse F-31062, France*

Christian Dussarrat – *Air Liquide Japan, Innovation Campus Tokyo, Yokosuka-shi, Kanagawa 239-0847, Japan*

Brigitte Caussat – *Laboratoire de Génie Chimique (LGC), Toulouse F-31062, France; INP, Toulouse F-31400, France; Université Toulouse III, Toulouse F-31062, France; CNRS, délégation Occitanie Ouest du CNRS, Toulouse F-31062, France;* orcid.org/0000-0003-4238-2919

Viviane Turq – *Centre Interuniversitaire de Recherche et d'Ingénierie des Matériaux (CIRIMAT), Toulouse F-31062, France; INP, Toulouse F-31400, France; Université Toulouse III, Toulouse F-31062, France; CNRS, délégation Occitanie Ouest du CNRS, Toulouse F-31062, France*

Constantin Vahlas – *Centre Interuniversitaire de Recherche et d'Ingénierie des Matériaux (CIRIMAT), Toulouse F-31062, France; INP, Toulouse F-31400, France; Université Toulouse III, Toulouse F-31062, France; CNRS, délégation Occitanie Ouest du CNRS, Toulouse F-31062, France;* orcid.org/0000-0001-5911-0296

Complete contact information is available at:
https://pubs.acs.org/10.1021/acsaenm.3c00584

Author Contributions

The manuscript was written through contributions of all authors. All authors have given approval to the final version of the manuscript.

Notes

The authors declare no competing financial interest.

■ ACKNOWLEDGMENTS

The present work was funded by ANR (Agence Nationale de la Recherche) under the contract HEALTHYGLASS ANR-17-CE08-0056. The authors acknowledge ANR for supporting the present research. This work benefited from the facilities of the platform MACLE-CVL, cofunded by the European Union and Centre-Val de Loire Region (FEDER). The authors are indebted to Claire Tendero (CIRIMAT) for AFM measurements, to Claudie Josse (UMS Castaing) for the preparation of FIB lamellas, and to the CaSciModOT Project (Calcul

Scientifique et Modélisation à Orléans et Tours) for access to high-performance computing facilities.

REFERENCES

(1) Zadbuke, N.; Shahi, S.; Gulecha, B.; Padalkar, A.; Thube, M. Recent trends and future of pharmaceutical packaging technology. *J. Pharm. BioAllied Sci.* **2013**, *5*, 98−110.

(2) Ghorpade, K. B.; Shinde, S. M. Glass Delamination in sterile formulations and Drug Recalls: A Review. *Int. J. Pharm. Sci. Dev. Res.* **2022**, *8*, 1−5.

(3) Lowe, D. *Materials and Gases, Vials and Vaccines, in Covid-19*; AAAS: Washinton, DC, 2020.

(4) Hellmann, R.; Cotte, S.; Cadel, E.; Malladi, L.; Karlsson, L. S.; Lozano-Perez, S.; Cabié, M.; Seyeux, A. Nanometre-scale evidence for interfacial dissolution−reprecipitation control of silicate glass corrosion. *Nat. Mater.* **2015**, *14*, 307−311.

(5) Etchepare, P. L.; Samélor, D.; Vergnes, H.; Caussat, B.; Vahlas, C. Barrier properties and hydrothermal aging of amorphous alumina coatings applied on pharmaceutical vials. *Surf. Coat. Technol.* **2021**, *425*, No. 127711.

(6) Collin, M.; Diallo, B.; Lecoq, H.; Ory, S.; Chauvet, E.; Pellerin, N. Chemical durability of lead crystal glass: Comparison of short-term aqueous and atmospheric alteration at 90°C. *Int. J. Appl. Glass Sci.* **2021**, *12*, 158−174.

(7) Doret, A.; Pellerin, N.; Allix, M.; Pellerin, S.; Lena, V.; Perrigaud, K.; Massiot, D. Influence of Alteration Solutions on the Chemical Durability of the Zerodur Glass-Ceramic: Structural Investigation. *Int. J. Appl. Ceram. Technol.* **2015**, *12*, 811−824.

(8) Gin, S.; Delaye, J.-M.; Angeli, F.; Schuller, S. Aqueous alteration of silicate glass: state of knowledge and perspectives. *npj Mater. Degrad.* **2021**, *5*, No. 42.

(9) Sacha, G. A.; Saffell-Clemmer, W.; Abram, K.; Akers, M. J. Practical fundamentals of glass, rubber, and plastic sterile packaging systems. *Pharm. Dev. Technol.* **2010**, *15*, 6−34.

(10) Schaut, R. A.; Weeks, W. P. Historical review of glasses used for parenteral packaging. *J. Pharm. Sci. Technol.* **2017**, *71*, 279−296.

(11) Iacocca, R. G.; Toltl, N.; Allgeier, M.; Bustard, B.; Dong, X.; Foubert, M.; Hofer, J.; Peoples, S.; Shelbourn, T. Factors affecting the chemical durability of glass used in the pharmaceutical industry. *AAPS PharmSciTech* **2010**, *11* (3), 1340−1349.

(12) Ditter, D.; Nieto, A.; Mahler, H-C.; Roehl, H.; Wahl, M.; Huwyler, J.; Allmendinger, A. Evaluation of Glass Delamination Risk in Pharmaceutical 10 mL/10R Vials. *J. Pharm. Sci.* **2018**, *107*, 624−637.

(13) Ponton, S.; Dhainaut, F.; Vergnes, H.; Samélor, D.; Sadowski, D.; Rouessac, V.; Lecoq, H.; Sauvage, T.; Caussat, B.; Vahlas, C. Investigation of the densification mechanisms and corrosion resistance of amorphous silica films. *J. Non-Cryst. Solids* **2019**, *515*, 34−41.

(14) Diallo, B.; Topka, K. C.; Puyo, M.; Lebesgue, C.; Genevois, C.; Laloo, R.; Samélor, D.; Lecoq, H.; Allix, M.; Vergnes, H.; Senocq, F.; Florian, P.; Sarou-Kanian, V.; Sauvage, T.; Menu, M-J.; Caussat, B.; Turq, V.; Vahlas, C.; Pellerin, N. Network hydration, ordering and composition interplay of chemical vapor deposited amorphous silica films from tetraethyl orthosilicate. *J. Mater. Res. Technol.* **2021**, *13*, 534−547.

(15) Topka, K. C.; Babacar, D.; Samélor, D.; Laloo, R.; Sadowski, D.; Genevois, C.; Sauvage, T.; Senocq, F.; Vergnes, H.; Turq, V.; Pellerin, N.; Caussat, B.; Vahlas, C. Tunable SiO_2 to SiO_xC_yH films by ozone assisted chemical vapor deposition from tetraethylorthosilicate and hexamethyldisilazane mixtures. *Surf. Coat. Technol.* **2021**, *407*, No. 126762.

(16) AG, S. SCHOTT TopLine Options for Superior Shelf Life, 2023. https://www.schott.com/fr-fr/products/vials-p1000365/product-variants?tab=type-1-plus.

(17) Walther, M. *Thin Films on Glass*; Bach, H.; Krause, D., Eds.; Springer-Verlag GmbH, 2003; Vol. *67*, pp 373−379.

(18) Klause, M.; Rothhaar, U.; Bicker, M.; Ohling, W. Dissolution of thin SiO_2-coatings—Characterization and evaluation. *J. Non-Cryst. Solids* **2010**, *356*, 141−146.

(19) Hunt, D. *Evaluation of the Inner Surface Durability of Glass Containers*; Pharmacopeial Forum, 2012; Vol. *38*, pp 92−101.

(20) Rothaar, U.; Klause, M.; Hladik, B. Comparative delamination study to demonstrate the impact of container quality and nature of buffer system. *J. Pharm. Sci. Technol.* **2016**, *70* (6), 560−567.

(21) Bunker, B. C. Molecular mechanisms for corrosion of silica and silicate glasses. *J. Non-Cryst. Solids* **1994**, *179*, 300−308.

(22) Gritsenko, V. A.; Xu, J. B.; Kwok, R. W. M.; Ng, Y. H.; Wilson, I. H. Short range order and the nature of defects and traps in amorphous silicon oxynitride governed by the Mott rule. *Phys. Rev. Lett.* **1998**, *81*, 1054−1057.

(23) Ding, W.; Li, L.; Zhang, L.; Ju, D.; Peng, S.; Chai, W. An XPS study on the chemical bond structure at the interface between SiOxNy and N doped polyethylene terephthalate. *J. Chem. Phys.* **2013**, *138* (10), No. 104706.

(24) Kuiper, A. E. T.; Willemsen, M. F. C.; Vanijzendoorn, L. J. Hydrogen incorporation in silicon (oxy)nitride thin-films. *Appl. Phys. Lett.* **1988**, *53* (22), 2149−2151.

(25) Patil, J. J.; Reese, M. L.; Lee, E.; Grossman, J. C. Oxynitride-encapsulated silver nanowire transparent electrode with enhanced thermal, electrical, and chemical stability. *ACS Appl. Mater. Interfaces* **2022**, *14* (3), 4423−4433.

(26) Kaghouche, B.; Mansour, F.; Molliet, C.; Rousset, B.; Temple-Boyer, P. Investigation on optical and physico-chemical properties of LPCVD SiOxNy thin films. *Eur. Phys. J.: Appl. Phys.* **2014**, *66* (2), 20301.

(27) Topka, K. C.; Diallo, B.; Puyo, M.; Papavasileiou, P.; Lebesgue, C.; Genevois, C.; Tison, Y.; Charvillat, C.; Samélor, D.; Laloo, R.; Sadowski, D.; Senocq, F.; Sauvage, T.; Vergnes, H.; Menu, M-J.; Caussat, B.; Turq, V.; Pellerin, N.; Vahlas, C. Critical level of nitrogen incorporation in silicon oxynitride films: Transition of structure and properties, towards enhanced anticorrosion performance. *ACS Appl. Electron. Mater.* **2022**, *4*, 1741−1755.

(28) Charpentier, T.; Okhotnikov, K.; Novikov, A. N.; Hennet, L.; Fischer, H. E.; Neuville, D. R.; Florian, P. Structure of Strontium Aluminosilicate Glasses from Molecular Dynamics Simulation, Neutron Diffraction, and Nuclear Magnetic Resonance Studies. *J. Phys. Chem. B* **2018**, *122*, 9567−9583.

(29) Du, J.; Rimsza, J. M. Atomistic computer simulations of water interactions and dissolution of inorganic glasses. *npj Mater. Degrad.* **2017**, *1*, No. 16.

(30) Mahadevan, T. S.; Du, J. Evaluating water reactivity at silica surfaces using reactive potentials. *J. Phys. Chem. C* **2018**, *122*, 9875−9885.

(31) Topka, K. C.; Vergnes, H.; Tsiros, T.; Papavasileiou, P.; Decosterd, L.; Diallo, B.; Senocq, F.; Samélor, D.; Pellerin, N.; Menu, M.-J.; Vahlas, C.; Caussat, B. An innovative kinetic model allowing insight in the moderate temperature chemical vapor deposition of silicon oxynitride films from tris (dimethylsilyl)amine. *Chem. Eng. J.* **2022**, *431*, No. 133350.

(32) Cova, P.; Masut, R. A.; Grenier, O.; Poulin, S. Effect of unintentionally introduced oxygen on the electron−cyclotron resonance chemical-vapor deposition of SiN_x films. *J. Appl. Phys.* **2002**, *92*, 129−138.

(33) Volkov, V. T.; Satunkina, L. F. Influence of oxygen on the composition and some properties of the films obtained by r.f. sputtering from a Si_3N_4 target. *Thin Solid Films* **1994**, *247*, 145−147.

(34) Pliskin, W. A. Comparison of properties of dielectric films deposited by various methods. *J. Vac. Sci. Technol.* **1977**, *14*, 1064−1081.

(35) Young, T., III. An essay on the cohesion of fluids. *Philos. Trans. R. Soc. London* **1805**, *95*, 65−87.

(36) Wenzel, R. N. Surface Roughness and Contact Angle. *J. Phys. Chem. A* **1949**, *53*, 1466−1467.

(37) Puyo, M.; Topka, K. C.; Diallo, B.; Laloo, R.; Genevois, C.; Florian, P.; Sauvage, T.; Samélor, D.; Senocq, F.; Vergnes, H.;

Caussat, B.; Menu, M-J.; Pellerin, N.; Vahlas, C.; Turq, V. Beyond surface nanoindentation: Combining static and dynamic nanoindentation to assess intrinsic mechanical properties of chemical vapor deposition amorphous silicon oxide (SiO_x) and silicon oxycarbide (SiO_xC_y) thin films. *Thin Solid Films* **2021**, *735*, No. 138844.

(38) Etchepare, P.-L.; Vergnes, H.; Samélor, D.; Sadowski, D.; Brasme, C.; Caussat, B.; Vahlas, C. Amorphous alumina coatings on glass bottles using direct liquid injection MOCVD for packaging applications. *Adv. Sci. Technol.* **2014**, *91*, 117−122.

(39) Unuma, H.; Kawamura, K.; Sawaguchi, N.; Maekawa, H.; Yokokawa, T. Molecular-dynamics study of Na-Si-O-N oxynitride glasses. *J. Am. Ceram. Soc.* **1993**, *76* (5), 1308−1312.

(40) Todorov, I. T.; Smith, W.; Trachenko, K.; Dove, M. T. DL_POLY_3: new dimensions in molecular dynamics simulations via massive parallelism. *J. Mater. Chem.* **2006**, *16*, 1911−1918.

(41) Clark, S. J.; Segall, M. D.; Pickard, C. J.; Hasnip, P. J.; Probert, M. I. J.; Refson, K.; Payne, M. C. First principles methods using CASTEP. *Z. Kristallogr. - Cryst. Mater.* **2005**, *220*, 567−570.

(42) Perdew, J. P.; Burke, K.; Ernzerhof, M. Generalized gradient approximation made simple. *Phys. Rev. Lett.* **1996**, *77*, 3865−3868.

(43) Yates, J. R.; Pickard, C. J.; Mauri, F. Calculation of NMR chemical shifts for extended systems using ultrasoft pseudopotentials. *Phys. Rev. B* **2007**, *76*, No. 024401.

(44) Giorgis, F.; Giuliani, F.; Pirri, C. F.; Tresso, E.; Summonte, C.; Rizzoli, R.; Galloni, R.; Desalvo, A.; Rava, P. Optical, structural and electrical properties of device-quality hydrogenated amorphous silicon-nitrogen films deposited by plasma-enhanced chemical vapour deposition. *Philos. Mag. B* **1998**, *77*, 925−944.

(45) Peter, S.; Bernütz, S.; Berg, S.; Richter, F. FTIR analysis of a-SiCN:H films deposited by PECVD. *Vacuum* **2013**, *98*, 81−87.

(46) Behrens, K. M.; Klinkenberg, E. D.; Finster, J.; Meiwes-Broer, K. H. Geometric structure of thin Si_Ox_Ny films on Si(100). *Surf. Sci.* **1998**, *402−404*, 729−733.

(47) Shahpanah, M.; Mehrabian, S.; Abbasi-Firouzjah, M.; Shokri, B. Improving the oxygen barrier properties of PET polymer by radio frequency plasma-polymerized SiO_xN_y thin film. *Surf. Coat. Technol.* **2019**, *358*, 91−97.

(48) Yonekura, D.; Fujikawa, K.; Murakami, R.-I. Influence of film structure on gas barrier properties of SiO_xN_y films. *Surf. Coat. Technol.* **2010**, *205*, 168−173.

(49) Feuston, B. P.; Garofalini, S. H. Topological and bonding defects in vitreous silica surfaces. *J. Chem. Phys.* **1989**, *91*, 564−570.

(50) Gritsenko, V. A. Atomic structure of the amorphous nonstoichiometric silicon oxides and nitrides. *Phys.-Usp.* **2008**, *51* (7), 699−708.

(51) Shi, Y.; Neuefeind, J.; Ma, D.; Page, K.; Lamberson, L. A.; Smith, N. J.; Tandia, A.; Song, A. P. Ring size distribution in silicate glasses revealed by neutron scattering first sharp diffraction peak analysis. *J. Non-Cryst. Solids* **2019**, *516*, 71−81.

(52) Martinet, C.; Heili, M.; Martinez, V.; Kermouche, G.; Molnar, G.; Shcheblanov, N.; Barthel, E.; Tanguy, A. Highlighting the impact of shear strain on the SiO2 glass structure: From experiments to atomistic simulations. *J. Non-Cryst. Solids* **2020**, *533*, No. 119898.

(53) Du, J.; Cormack, A. N. The medium range structure of sodium silicate glasses: a molecular dynamics simulation. *J. Non-Cryst. Solids* **2004**, *349*, 66−79.

(54) Murakami, M.; Sakka, S. Ab initio molecular orbital calculation of the interatomic potential and force constants in silicon oxynitride glass. *J. Non-Cryst. Solids* **1988**, *101*, 271−279.

(55) Sakka, S. Structure, properties and application of oxynitride glasses. *J. Non-Cryst. Solids* **1995**, *181*, 215−224.

https://doi.org/10.1021/acsaenm.3c00584